# **Diffuse-Denoise-Count: Accurate Crowd-Counting with Diffusion Models**

Yasiru Ranasinghe, Nithin Gopalakrishnan Nair, Wele Gedara Chaminda Bandara, and Vishal M. Patel Johns Hopkins University, Baltimore, USA

{dranasi1, ngopala2, wbandar1, vpatel36}@jhu.edu

### **Abstract**

Crowd counting is a key aspect of crowd analysis and has been typically accomplished by estimating a crowddensity map and summing over the density values. However, this approach suffers from background noise accumulation and loss of density due to the use of broad Gaussian kernels to create the ground truth density maps. This issue can be overcome by narrowing the Gaussian kernel. However, existing approaches perform poorly when trained with such ground truth density maps. To overcome this limitation, we propose using conditional diffusion models to predict density maps, as diffusion models are known to model complex distributions well and show high fidelity to training data during crowd-density map generation. Furthermore, as the intermediate time steps of the diffusion process are noisy, we incorporate a regression branch for direct crowd estimation only during training to improve the feature learning. In addition, owing to the stochastic nature of the diffusion model, we introduce producing multiple density maps to improve the counting performance contrary to the existing crowd counting pipelines. Further, we also differ from the density summation and introduce contour detection followed by summation as the counting operation, which is more immune to background noise. We conduct extensive experiments on public datasets to validate the effectiveness of our method. Specifically, our novel crowd-counting pipeline improves the error of crowd-counting by up to 6% on JHU-CROWD++ and up to 7% on UCF-QNRF. The project will be available at github.com/dylran/DiffuseDenoiseCount.

# 1. Introduction

Crowd counting has been a key element in surveillance, public safety, and crowd control. Various methods have been proposed in the literature to estimate the count including methods that directly predict the count [21, 51, 56] or use a surrogate task such as density estimation [14, 17, 46, 47, 49, 50], object detection [29, 37], or

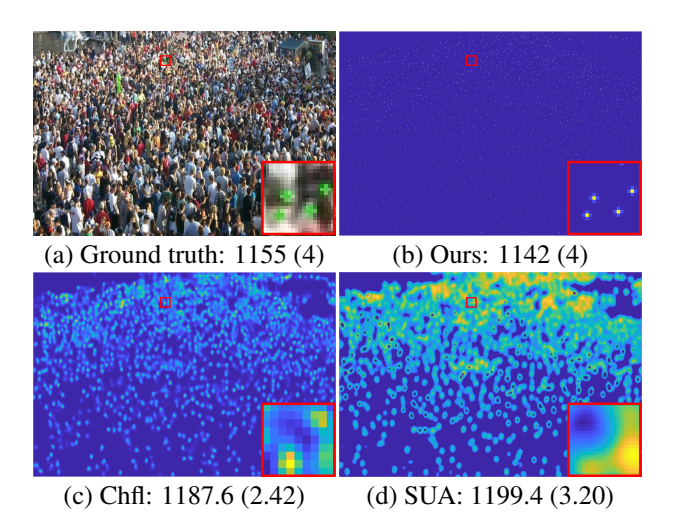


Figure 1. Predicted density results for (a) a dense crowd from (b) our method, (c) Chfl [41], and (d) SUA [32]. The count of the enlarged crop is given in brackets.

point localization [11, 22, 45, 54]. In recent state-of-the-art (SOTA) methods, density estimation, and point localization have been frequently used.

While density-based methods sum the estimated pixel density values for counting [14], localization-based methods count proposals with confidence scores higher than a threshold [45]. As a result, density-based methods are more susceptible to introducing background noise into the final count compared to localization-based methods [48]. Furthermore, density estimation methods are affected by variations in crowd density distributions, that arise due to different congestion levels of the crowd [4]. This could result in a loss of accuracy in the density estimation. In contrast, recent localization-based methods with point queries do not have the issue of background noise accumulation [22], like in density-based methods [41], as there is no interference between neighboring point proposals. However, localization-based methods require crowd-density heuristics for proposal setting [45], which is not required by density-based methods. Thus, if the premise of point supervision is translated into density-based methods, it is possible to circumvent the requirement for crowd-density heuristics as well as the flaws of conventional density-based methods, and a narrow-density kernel can be used to achieve this. However, Xu et al. [54] demonstrated that using a narrow kernel is ineffective with density regression methods.

Alternatively, it is feasible to use a generative model to predict the density map of a given crowd image that would learn the distribution of the values in the density map. Though GAN-based architectures have been used for density map prediction [10, 40, 55], these methods still rely upon broad kernel sizes and overlook the benefits of point supervision. Since the model learns the distribution of the density pixel values, it is advantageous to maintain the sample space of the density pixel values, and employing a broad kernel will only discourage it. Furthermore, the use of both point supervision and crowd density prediction with generative models has not been fully investigated before. Also, the aforementioned GAN-based approaches restrict to a single crowd-density map realization similar to the regressionbased methods and jettison the stochastic nature of generative models to produce multiple density map realizations which could improve the counting performance.

To that end, we propose to use denoising diffusion probabilistic models (referred to as diffusion models), [13, 34] to generate crowd density maps for a given image. Though, diffusion models have been applied to segmentation [3, 12], super-resolution [18], object detection [6], etc., to the best of our knowledge, neither crowd-counting nor density map generation has been studied with diffusion models. Furthermore, we exercise our desired narrow Gaussian kernel into practice by constructing the ground truth crowd-density maps for training the denoising diffusion process. With the narrow kernel, we minimize the interference between adjacent densities which helps maintain the bounds and the distribution of density pixel values. This in turn simplifies the distribution learning for the diffusion model and improves density prediction as illustrated in Fig. 1 where the proposed method has reproduced the narrow kernel even in a dense region while the other two methods have failed.

Additionally, to eschew the loss of density that is probable with the density-based crowd-counting methods, we simply count the number of blobs observed in the predicted density map and this is done by detecting the contours in the map. Consequently, we eliminate the effect of background noise as there is no requirement to sum over the density pixel values. Then, we introduce the crowd map fusion mechanism where multiple dot maps constructed by detecting contours are combined together to improve the counting performance. It is noteworthy that this is only possible with generative models due to their stochastic nature. In addition, inspired by Deja *et al.* [9] on joint learning with diffusion models, we introduce an auxiliary re-

gression branch only during training which estimates the crowd count based on encoder-decoder feature representations from the denoising network to improve feature learning.

In summary, our contributions are:

- We formulate crowd-density map generation as a denoising diffusion process. To the best of our knowledge, this is the first study to perform crowd counting with diffusion models.
- We promote the idea of using a narrow Gaussian kernel to ease the learning process and to facilitate the high-quality density map generation with more fidelity to the ground truth Gaussian kernel.
- We introduce counting via contour detection made possible by the use of narrow kernels as opposed to the summation of pixels.
- We propose a mechanism to consolidate multiple crowd density realizations into a single result to improve counting performance utilizing the stochastic nature of diffusion models.
- We show that the proposed method surpasses the SOTA performance on public crowd-counting datasets.

### 2. Related works

### 2.1. Crowd counting

Localization-based methods perform counting by predicting the locations of people. Primarily, it was performed as an object detection task [20, 29, 37] that involves predicting a bounding box about heads. Since most datasets provide head locations, ground truth bounding boxes are created using data heuristics [58]. Hence, inaccurate bounding boxes will frustrate the learning process and increase false detection with non-maximum suppression [45]. To circumvent this, other methods perform localization by points [20] or blobs [27], yet do not remove duplicates in congested regions during post-processing. Hence, recent query-based localization methods [22, 45] for crowd-counting circumvent any post-processing with one-to-one matching to estimate the point locations of individuals inspired by DETR [5]. However, these methods still require point proposals [45] or queries [22] which should be initialized using data statistics of the crowd density which does not exactly resolve the reliance on data heuristics.

**Density-based methods** [4, 19, 25, 26, 28, 33, 53] attempt to produce a density map for a given crowd image and then obtain the count by summing over the predicted density maps. Unlike localization-based methods, density regression methods do not require any statistics other than the crowd locations [48]. But, density-based methods suffer from background noise and loss of density [30, 31, 35] in congested regions due to the use of broad kernels dur-

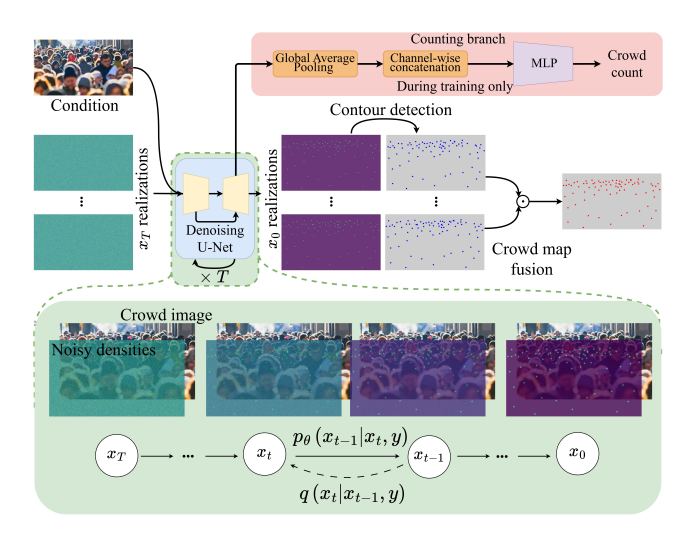


Figure 2. Overall crowd-counting pipeline. The crowd density maps are generated from the denoising diffusion process for a crowd image. Next, contour detection is performed on the resulting crowd density realizations to create crowd maps. The crowd maps are then fused into a single crowd map. The counting branch is trained in parallel using the encoder-decoder features of the denoising U-Net and discarded during inference.

ing training. Nonetheless, it is ineffective to use a narrow Gaussian kernel to generate ground truths as experimentally shown by [54] with regression networks. Hence, we treat the prediction of the density map as a generative task where the distribution of the density values is learned by conditioning on different crowd images inspired by [10,40,55].

#### 2.2. Diffusion models for crowd-density generation

Diffusion models are a class of likelihood-based models inspired by non-equilibrium thermodynamics [43]. These generative models are defined based on a Markov chain with a forward and a reverse process. In the forward process, noise is gradually added to data; and is denoised in the reverse process. The forward process is formulated as,

$$q(\mathbf{x_t}|\mathbf{x_{t-1}}) = \mathcal{N}(\mathbf{x_t}|\sqrt{1-\beta_t}\mathbf{x_{t-1}}, \beta_t \mathbf{I}), \quad (1)$$

where the sample datum  $\mathbf{x_0}$  is gradually transformed to a noisy sample  $\mathbf{x_t}$  for  $t \in \{1,\ldots,T\}$  by adding Gaussian noise according to a noise variance schedule  $\beta_1,\ldots,\beta_T$ . Here  $\mathbf{I}$  is the identity matrix. Nonetheless,  $\mathbf{x_t}$  can be computed using  $\mathbf{x_0}$  and a noise vector  $\epsilon \sim \mathcal{N}(\mathbf{0},\mathbf{I})$  and with the forward transformation,

$$\mathbf{x_t} = \sqrt{\bar{\alpha}_t} \mathbf{x_0} + (1 - \bar{\alpha}_t) \epsilon, \qquad (2)$$

where  $\bar{\alpha}_t := \prod_{\tau=1}^t \alpha_\tau = \prod_{\tau=1}^t (1 - \beta_\tau)$  and  $\beta_\tau$ .

In this work, we aim to perform crowd-density map generation via the diffusion model. Hence, our data samples

will be crowd-density maps  $\mathbf{x_0} \in \mathbb{R}^{H \times W}$ , where H and W are the height and width dimensions. However, in lieu of training a neural network to predict  $\mathbf{x_0}$  from  $\mathbf{x_t}$  for various time steps, we predict the amount of noise  $(\hat{\epsilon})$  in  $\mathbf{x_t}$  at each time step conditioned on the crowd image  $(\mathbf{y})$ , and apply the reverse diffusion process to obtain  $\mathbf{x_0}$  ultimately.

To that end, to train the denoising diffusion network, we use the hybrid loss  $(L_{hybrid})$  function proposed by Nichol *et al.* in [34]. To promote learning coarse features at lower SNR stages, we adopt the weighting scheme [8] defined as,

$$\lambda_t = \frac{(1 - \beta_t)(1 - \bar{\alpha_t})/\beta_t}{(k + \text{SNR}(t))^{\gamma}}, \text{ where } \text{SNR}(t) = \frac{\bar{\alpha_t}}{1 - \bar{\alpha_t}}$$
 (3)

with k and  $\gamma$  as hyperparameters. Hence, the final loss over which the denoising network is optimized is defined as follows,

$$L_{hybrid} = \mathbf{E}_{\mathbf{x}_{0},\mathbf{y},\epsilon} \left[ \lambda_{t} \| \hat{\epsilon}_{(\mathbf{x}_{0},\mathbf{y},t)} - \epsilon \|_{2}^{2} \right] + \lambda_{vlb} L_{vlb}, \quad (4)$$

where  $L_{vlb}$  is the original variational lower bound defined in [34] and  $\lambda_{vlb}$  is its weighting factor.

# 3. Proposed approach

In this section, we first review the motivation for selecting an appropriate kernel size. Following, we present the joint learning of counting as an auxiliary task to improve the density map generation performance. Finally, we introduce a method to combine different realizations for density maps to improve crowd-counting performance. The overall crowd-counting pipeline is illustrated in Fig. 2.

#### 3.1. An extremely narrow kernel

The diffusion process requires a density map to learn the conditional distribution of crowd density. The crowd density map can be acquired by convolving point information with a pre-defined Gaussian kernel. For that, it is important to select a proper kernel size and a variance as it governs the distribution of the pixel values of the crowd-density maps.

As demonstrated in Fig. 3, the divergence between the distribution of the Gaussian kernel (values) and the resulting density map increases as the kernel size and variance increase, especially for a densely crowded scene. While this might not be the case for sparse crowd scenes as there is minimal or no interference between density kernels. However, this implies that the density pixel value distribution is highly image dependent which hinders the learning of the crowd densities. This can be eschewed by narrowing the distribution of the Gaussian kernel as illustrated in Fig. 3. This also helps the denoising diffusion network to maintain the pixel values within a pre-defined range. The difference between the probability mass of a broad Gaussian kernel and the resulting density map is significant. This can lead

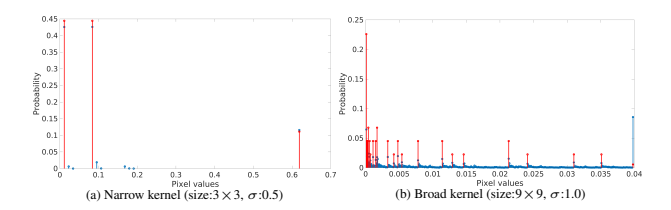


Figure 3. Change in the pixel values of the Gaussian kernel (red stems) and the resulting density map (blue stems) for a crowd image with a 3,547 crowd count. The kernel size and variance increase from left to right.

to the clipping of many pixel values, resulting in a loss of information in congested scenes.

The aforementioned issue can be solved by a narrow kernel. A narrow kernel provides an alternative path to crowd counting without summing over the density map values. As shown in Fig. 1, the crowd count can be obtained by simply counting the observable kernels. For that, we perform contour detection on the density maps and obtain the location of each kernel. Then, the crowd count is computed as the total number of locations. This provides the means to avoid background noise in the generated density maps and to obtain the crowd count by detecting these narrow kernels in the crowd-density maps. Unlike the local maxima detection strategy proposed in [23] to detect head locations from a crowd-density map, our method is not dependent on any hyperparameter tuning for contour detection.

# 3.2. Joint learning of counting

Direct regression of the crowd count from image features is a harder task [21] compared to counting with a surrogate task. To perform the direct computation of the crowd count we consider the intermediate features of the encoder and the decoder of the denoising U-Net. Let's denote the set of intermediate features from the denoising network for a particular timestep t as  $\mathcal{Z}_t = \{\mathbf{z}_t^1, \mathbf{z}_t^2, \dots, \mathbf{z}_t^d\}$ , where  $\mathbf{z}_t^*$  is the representation vector at the corresponding feature level of the decoder (see Fig. 5). Since the spatial dimensions of the intermediate representations at different depth levels are incompatible, global average pooling is performed on each  $\mathbf{z}_t^*$  which are then concatenated to construct a single feature vector  $\mathbf{z}_t$ . This is then passed through the regression network to estimate the crowd count.

However, for a sampled pair  $(\mathbf{x_0}, \mathbf{y})$ , only the density map  $\mathbf{x_0}$  is diffused with noise according to a noise schedule. Hence, the noise level in the set of intermediate features  $\mathcal{Z}_t$  will vary with the timestep, and SNR will be lower in the later stages of the diffusion process than in the earlier stages. Hence, we utilize the weighting scheme discussed in Section 2.2 during the training of the count regression

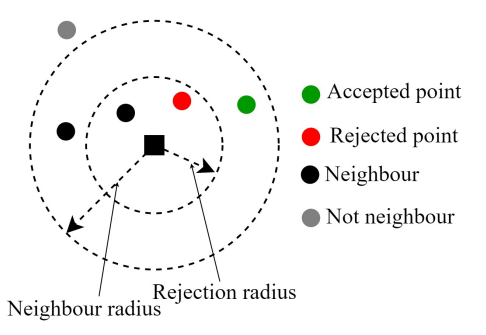


Figure 4. Crowd map fusion criterion. The rejection radius is computed from the neighbors (black) inside the neighbor radius. New points (colored) that fall inside the rejection radius are removed (red) and the rest (green) are combined into the compound map.

network. We utilize  $L_1$ -loss as follows,

$$L_1^t = \lambda_t \|\bar{c}_t - c\|_1 \tag{5}$$

to measure the difference between the prediction  $(\bar{c}_t)$  and the ground truth (c) for a given time step t and a given sampled pair, where  $\lambda_t$  is the same weighting factor used in Eqn. (3). As the training loss for the denoising model is the Monte-Carlo approximation of the sum over all timesteps, the training loss can be written as

$$L_{count} = \mathbb{E}_{\mathbf{x}_0, \mathbf{y}, t} \left[ \lambda_t \| \bar{c}_t - c \|_1 \right]. \tag{6}$$

### 3.3. Overall training objective

The overall training includes optimization over the parameters of the denoising network and the regression branch. Hence, the overall training objective is as follows,

$$L_{overall} = L_{hybrid} + \lambda_{count} L_{count}, \tag{7}$$

where  $\lambda_{count}$  is a weightage on the counting task.

# 3.4. Stochastic crowd map fusion

The stochastic nature of the diffusion models could generate different realizations of the crowd-density map for the same crowd image. Therefore, the counting performance with diffusion models can be improved with multiple realizations contrary to the traditional crowd-counting methods as evidenced by other tasks based on diffusion models such as segmentation [12] and detection [6]. However, rather than averaging individual counts from different realizations, they could be combined to compute a more improved count because individual realizations could infer crowd densities that were not present in other realizations.

To combine different realizations for the crowd-density maps, only the new information should be transferred to the compound crowd-density map. For that, we first compute

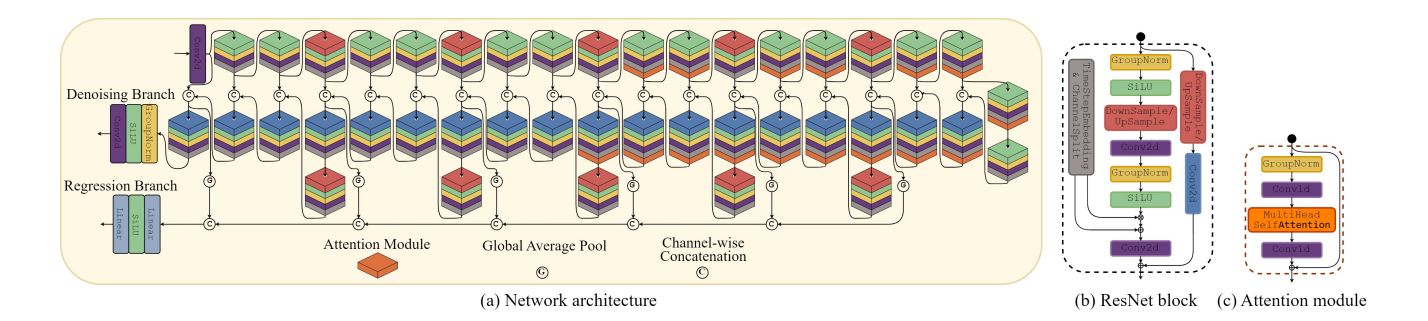


Figure 5. (a) **Network architecture** for the denoising U-Net in conjunction with the count regression branch and the basic modules, (b) **ResNet block** and (c) **Attention module**, used to construct the network. Each cuboid in a stack represents the functioning modules in the ResNet Block and whether the attention module is applied. **Top stacks** are in the encoder. **Bottom stacks** are in the decoder

the locations of the density kernels by applying contour detection. Once these locations are found, a dot map is constructed for each density map, referred to as the 'crowd map'. Then, we consider the dissimilarity between the crowd maps from different realizations and to measure that we consider the structural similarity index measure (SSIM) [52]. For each crowd map we assign a similarity score measured as the cumulative of the SSIM with the remaining crowd map realizations. Then, the maps will be arranged in the ascending order of the SSIM before combining.

When fusing two crowd maps, it is necessary to reject repeating point locations. This is performed based on the locations of the new points compared to the points in the combined list. To start, we take the crowd map first in order and the head locations from that realization as the reference. Next, we define a rejection radius for each head location as:

$$r_n = \beta \frac{\sum_{i=1}^{\tilde{k}} r_{ni}}{2\tilde{k}} \tag{8}$$

by considering the k-nearest neighbors within a fixed range. Here  $\beta$  is a scaling factor and  $\tilde{k}$  is the total nearest neighbors within the range. Next, we remove the head locations of the next crowd map locations that fall within the rejection radii in the reference map as illustrated in Fig. 4, and the remaining locations are added to the reference map. This procedure is performed until all realizations are exhausted.

# 4. Experimental details

**Denoising network** has a U-Net architecture [34] and each downsampling and upsampling layer scales the features by a factor of two along each spatial dimension. We use average pooling for downsampling with a  $2 \times 2$  kernel and a stride of 2, and nearest neighbor interpolation for upsampling. The 2-dimensional convolution layers are  $3 \times 3$  kernels with a stride of 1 and the 1-dimensional convolution layers have a kernel size and a stride of 1. The denoising network and the basic modules are illustrated in Fig. 5.

**Regression branch** is a lightweight network with linear layers and a Rectified Linear Unit (ReLU) [2] activation. We apply global average pooling to maintain compatibility along the spatial dimension for channel-wise concatenation. **Diffusion process** uses 1,000 timesteps and DDIM sampling [44] during inference. We use a linear noise schedule with noise variance ranging from  $1 \times 10^{-3}$  to 0.02.

Hyperparameter values  $\lambda_{count}$  is set as  $5 \times 10^{-3}$  to match the range of the value for  $L_{hybrid}$ . The  $\gamma$  and k values are set as 0.5 and 1, respectively to compute the SNR-based weighting factors. We adopt the original scaling factor of  $1 \times 10^{-3}$  for  $\lambda_{vlb}$  following [34]. For crowd map fusion, we set  $\beta$  equal to 0.85 and the maximum nearest neighbors to four. The radius for the neighbor search was restricted to 0.05 of the minimum of the image dimensions.

**Training** of the denoising network is initialized with the ImageNet pre-trained weights for the super-resolution [36] task except for the input and output layers. The network is trained for  $2\times 10^5$  iterations with a batch size of 8 for  $256\times 256$  images. We use an AdamW optimizer with a fixed learning rate  $1\times 10^{-4}$  and a linear warm-up schedule over  $5\times 10^3$  training steps.

**Ground truth density maps** are prepared by placing a 2-dimensional Gaussian kernel with a variance of 0.25 and a filter size of  $3 \times 3$ .

Inference for a given crowd image is performed by constructing non-overlapping image patches of size  $256 \times 256$ . For images, that are non-divisible by the crop dimension, overlapping crops are used for the remaining portions of the image, and these overlapping regions are removed when constructing the complete crowd-density maps. Further, we limit to four realizations for each crowd image to perform crowd map fusion.

**Evaluations** are performed on five public datasets: JHU-CROWD++ [42], ShanghaiTech A [57], ShanghaiTech B [57], UCF\_CC\_50 [15], and UCF-QNRF [16]. We use MAE and MSE as the performance metrics.

Method	Venue	JHU-CROWD++		ShanghaiTech A		ShanghaiTech B		UCF_CC_50		UCF-QNRF	
		MAE↓	MSE↓	MAE↓	MSE↓	MAE↓	MSE↓	MAE↓	MSE↓	MAE↓	MSE↓
ADSCNET	CVPR'20	-	-	55.40	97.70	6.40	11.30	198.40	267.30	71.30	132.50
SUA	ICCV'21	80.70	290.80	68.50	121.90	14.10	20.60	-	-	130.30	226.30
SASNet	AAAI'21	-	-	<u>53.59</u>	88.38	6.35	9.90	<u>161.40</u>	234.46	85.20	147.30
ChfL	CVPR'22	57.00	235.70	57.50	94.30	6.90	11.00	-	-	80.30	137.60
MAN	CVPR'22	<u>53.40</u>	209.90	56.80	90.30	-	-	-	-	77.30	<u>131.50</u>
GauNet	CVPR'22	58.20	245.10	54.80	89.10	6.20	9.90	186.30	256.50	81.60	153.70
CLTR	ECCV'22	59.50	240.60	56.90	95.20	6.50	10.60	-	-	85.80	141.30
Ours		49.44	204.71	52.87	85.62	6.08	9.61	157.12	220.59	65.79	126.53

Table 1. Comparison with the SOTA methods on JHU-CROWD++, ShanghaiTech A, ShanghaiTech B, UCF\_CC\_50, and UCF-QNRF datasets. The best results are shown in **bold**. The second-best results are underlined.

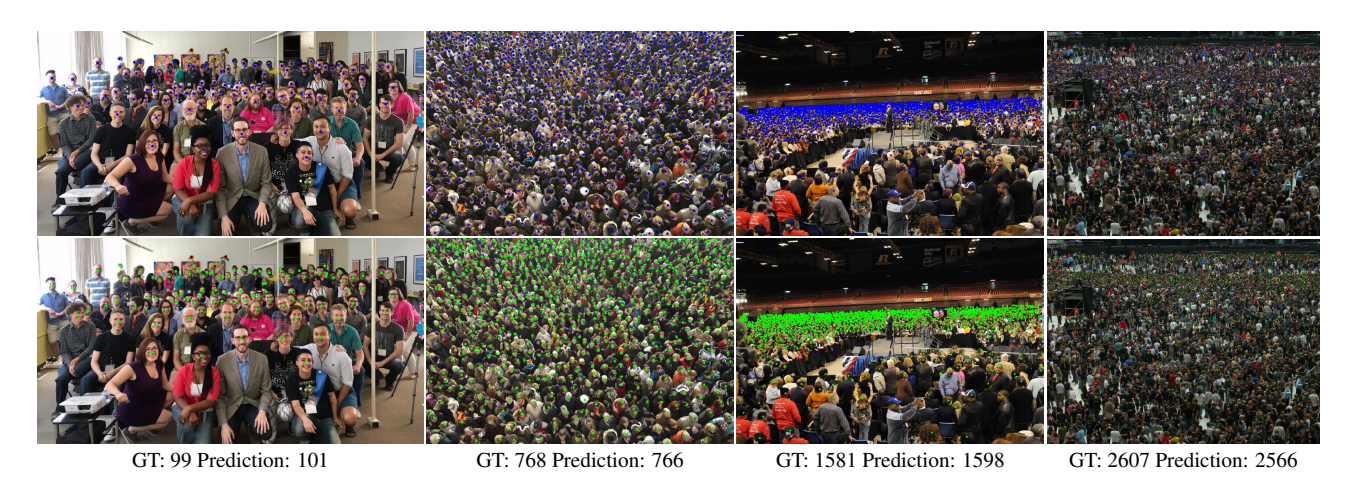


Figure 6. Qualitative results for the proposed method with the ground truths. The prediction is produced after combining multiple realizations.

### 5. Results

We extensively evaluate the performance of our method on publicly available crowd-counting datasets and compare it with the recent SOTA methods. We provide ablation studies for each aspect of the proposed crowd-counting pipeline.

#### 5.1. Crowd counting performance

Quantitative results for crowd counting are presented in Table 1 for the proposed method with other existing methods. The proposed method achieves SOTA crowd-counting results on public crowd-counting datasets, and the improvement can be explained by two factors. First, the proposed use of a narrow kernel has improved the counting results in dense regions by mitigating the loss of density values in contrast to conventional density-based methods. Second, we eliminate the effect of background noise on the crowd count, which scales with the image dimensions, by replacing density summation with contour detection followed by summation. Since JHU-CROWD++

and UCF-QNRF datasets contain dense crowd scenes and large image dimensions this explains the significant MAE margins of 6% and 7% for JHU-CROWD++ and UCF-QNRF, respectively, compared to the SOTA. This was possible due to the capability to produce accurate density maps with better resemblance to ground truth maps with diffusion models.

Qualitative results are presented in Fig. 1 and Fig. 6 for density map generation with diffusion models and crowd map generation with the proposed pipeline. As depicted in Fig. 1, the proposed method and the narrow kernel have the ability to accurately perform counting even in a dense region while the other two methods have suffered from loss of density. Further, our proposed pipeline has identified head locations accurately which is not possible with existing density-based methods, and without the need for data heuristics, unlike localization-based methods.

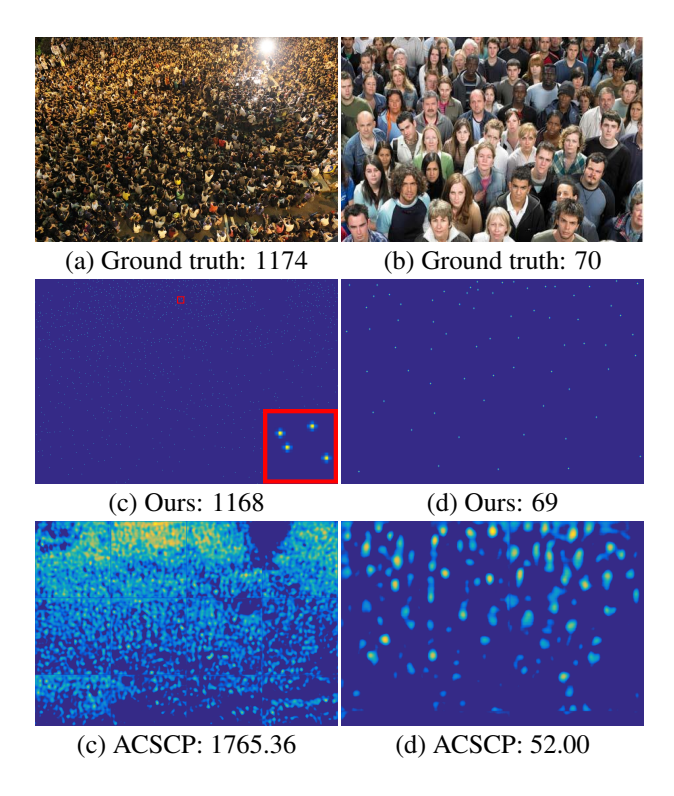


Figure 7. Generation quality and crowd performance comparison with a narrow kernel between the diffusion models and a GAN-based [40] method for different crowd scenes.

### 5.2. Ablation study

Diffusion models are considered to have more fidelity to training data than GAN-based methods. From Fig. 7 one can see that diffusion models have produced high-quality density maps with more accurate crowd counts while ASCSP [40], a GAN-based method, has failed. Furthermore, without the ability to produce narrow kernels in the predicted density maps, GAN-based methods have to use density summation as the counting operation which brings back the issues of noise accumulation and loss of density. This highlights the importance of using diffusion models for crowd-density map generation with contour detection as the counting operation.

**Stochastic crowd map** generation is a key benefit of diffusion-based generative models. In Fig. 8, we provide qualitative results of two realizations for each crowd image. From Fig. 8 we can see that different realizations have information that is not present in other realizations. Furthermore, it is noteworthy that using a narrow kernel facilitates the ability to produce new knowledge which can be included in the final prediction. Otherwise, novel information captured by different realizations will be diluted by averaging the density maps had a larger kernel been used. Though this is a generative model, the proposed method

Method		JHU-CROWD++		Shangha	aiTech B	UCF-QNRF	
	Method	MAE↓	MSE↓	MAE↓	MSE↓	MAE↓	MSE↓
.0	Best	52.56	215.01	6.25	9.91	72.39	131.98
0/w	Average	54.70	221.17	6.33	10.03	74.76	133.78
	Variance	1.6586	4.7822	0.0981	0.1528	2.2034	2.2348
/w	Best	50.46	209.05	6.17	9.76	68.86	128.49
\$	Average	50.80	209.66	6.20	9.81	69.73	129.53
	Variance	0.2664	0.8844	0.0222	0.0427	0.6106	0.6995

Table 2. Error metrics for individual realizations without (top half) and with (bottom half) the counting decoder.

Method	JHU-CR	OWD++	Shangha	iTech B	UCF-QNRF	
Method	MAE↓	MSE↓	MAE↓	MSE↓	MAE↓	MSE↓
Random	49.97	205.40	6.12	9.68	67.78	127.52
Ascend-SSIM	49.44	204.71	6.08	9.61	65.79	126.53
Descend-SSIM	50.32	208.79	6.15	9.73	68.44	127.98

Table 3. Comparison for crowd map fusion methods.

has reassigned densities perfectly in certain instances and for some cases, there is a slight shift in the location between realizations. This necessitates the need for the proposed crowd map fusion method since simply combing these shifted dots results in double counts and worsens the counting performance otherwise.

The counting branch is added to improve the counting performance with the crowd-density maps. We present the counting results for individual realizations with and without the regression network in Table 2. In specific, we consider the average error performance from different realizations to identify characteristic effects of the counting branch before combining them into a single crowd map. The addition of the counting branch has improved the average counting results, and the variation in the counting results has been reduced. This is because the counting branch promotes feature learning for intermediate time steps with noisy features as well. Furthermore, we provide a qualitative comparison between the feature maps of the denoising U-Net with and without the counting branch prediction for different time steps in Fig. 9. From Fig. 9 one can see that the decoder features are richer in detail for the case with the counting branch than without it. With the counting branch, the decoder generates features for the crowd starting from the initial time step. This is further clarified by the performance of the counting branch as the predicted count has not varied with time and deviated from the ground truth count significantly.

**Crowd map fusion** leverages the stochastic nature of the crowd-density maps produced by the diffusion process, and we adopt a systematic way to fuse the maps. In Table 3, we present the error metrics for three different methods:



Figure 8. Qualitative results for stochastic crowd map generation from two realizations. Green boxes include new dots created at different realizations. Blue boxes include dots that are present in both realizations but with a shift and pink boxes include perfectly reassigned dots. (best viewed in highest zooming level)

Method	JHU-CROWD++		Shangha	iTech A	UCF_CC_50	
Method	MAE↓	MSE↓	MAE↓	MSE↓	MAE↓	MSE↓
Contour detection	50.46	209.05	53.38	86.79	159.81	224.55
Density estimation	225.31	541.74	175.25	281.89	176.44	249.94
Noise residual	210.19	526.67	207.71	339.70	69.06	97.43

Table 4. Comparison between crowd counting operations and the effect of noise.

Random, Descend-SSIM, and Ascend-SSIM. In the Random method, we combine the maps in the order in which they are produced. In the Descend-SSIM method, we combine the maps in the order of decreasing similarity, and in the Ascend-SSIM method, we combine the maps in the order of increasing similarity as described in Section 3.4. The iterative improvement with stochastic generation and the proposed fusion method is shown in Fig. 10. From Table 3 we see that the counting performance has improved with the Descend method where more locally dissimilar realizations are combined initially. This observation is validated by the performance degradation with the Descend-SSIM method compared to the both Ascend-SSIM and Random methods. Contour detection is proposed as an alternative to density summation for the counting operation. The performance comparison between the two methods is tabulated in Table 4 for the best-performing realization of each dataset. From Table 4 we see that the density summation produces significantly inferior counting results than the contour detection despite both methods using the same density map. This is simply because of background noise accumulation with the summation operation and the proposed contour detection method displays better immunity to noise.

#### 6. Conclusions

In this work, we proposed a novel crowd-counting framework, where density map generation was treated as a denoising diffusion process. The new framework allows using extremely narrow density kernels with which noise can be suppressed more robustly in crowd-density maps. Furthermore, we implemented the counting operation by counting the density kernels rather than integrating the density map. For that, we performed contour detection on crowddensity maps which offered more immunity to noise than density summation. Also, the proposed method could iteratively improve the counting performance via multiple realizations, unlike other crowd-counting frameworks due to the stochastic nature of the generative models. Further, our proposed method assigns density kernels at head positions, unlike existing density-based methods, and without the need for data heuristics, like localization-based methods. Hence, we hope our work will provide a baseline and a novel perspective for both localization-based and densitybased crowd counting.

#### References

- [1] Shahira Abousamra, Minh Hoai, Dimitris Samaras, and Chao Chen. Localization in the crowd with topological constraints. In *Proceedings of the AAAI Conference on Artificial Intelligence*, volume 35, pages 872–881, 2021.
- [2] Abien Fred Agarap. Deep learning using rectified linear units (relu). *arXiv preprint arXiv:1803.08375*, 2018.
- [3] Tomer Amit, Eliya Nachmani, Tal Shaharbany, and Lior Wolf. Segdiff: Image segmentation with diffusion probabilistic models. *arXiv* preprint *arXiv*:2112.00390, 2021.
- [4] Shuai Bai, Zhiqun He, Yu Qiao, Hanzhe Hu, Wei Wu, and Junjie Yan. Adaptive dilated network with self-correction supervision for counting. In *Proceedings* of the IEEE/CVF conference on computer vision and pattern recognition, pages 4594–4603, 2020.
- [5] Nicolas Carion, Francisco Massa, Gabriel Synnaeve, Nicolas Usunier, Alexander Kirillov, and Sergey Zagoruyko. End-to-end object detection with transformers. In Computer Vision–ECCV 2020: 16th European Conference, Glasgow, UK, August 23–28, 2020, Proceedings, Part 1 16, pages 213–229. Springer, 2020.

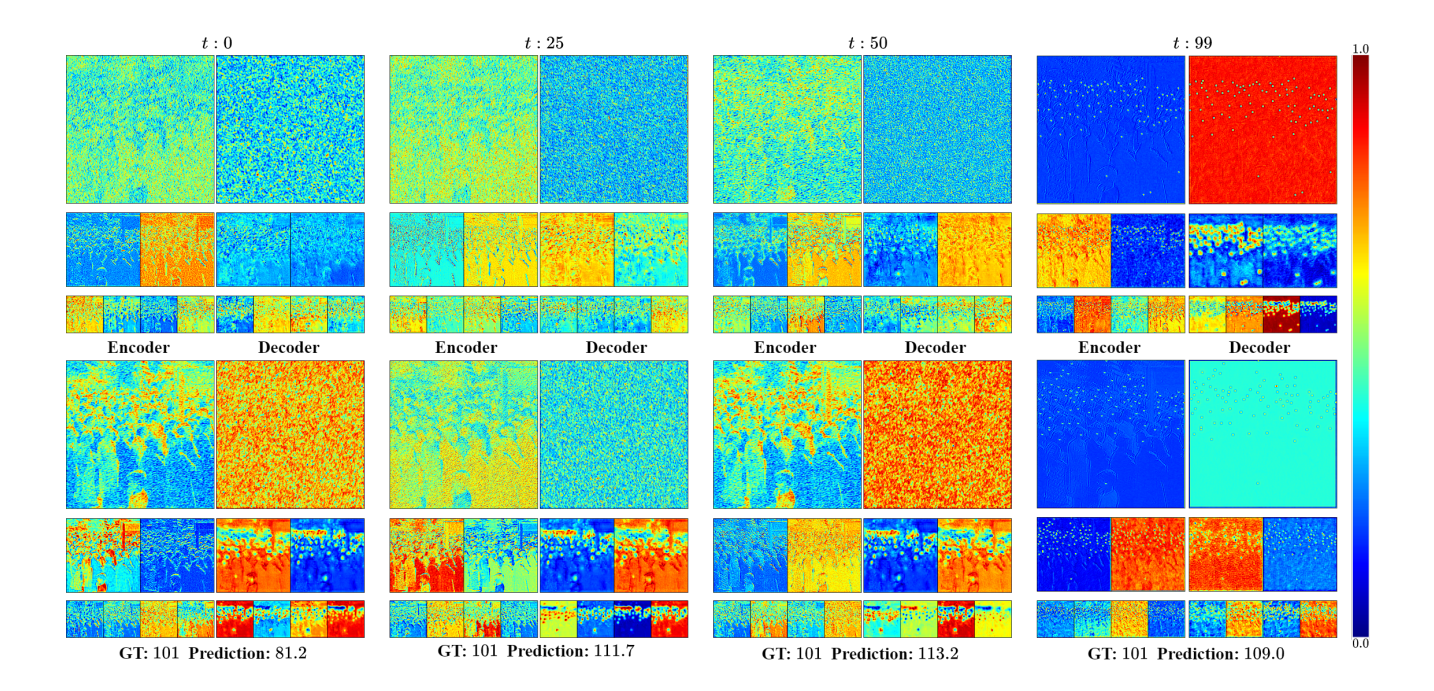


Figure 9. Encoder-Decoder feature maps produced by the denoising U-Net at different time steps. The **top row** feature maps are without the counting regression branch and the **bottom row** feature maps are with the regression branch. The feature maps are from the feature levels which are connected to the regression branch. The ground truth count for the  $256 \times 256$  image crop and the prediction from the counting branch at different time steps are given under each feature level.

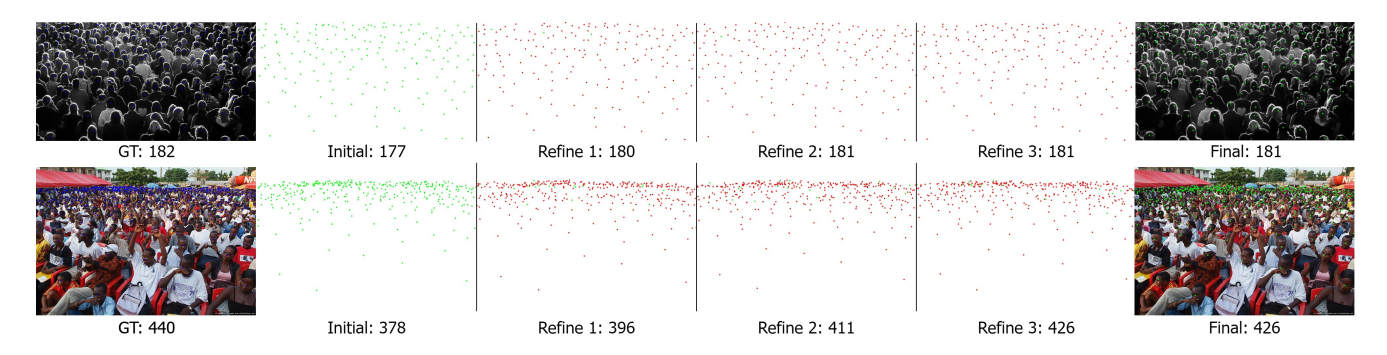


Figure 10. Qualitative results for the crowd-density map fusion method. Green dots represent the points combined to the final prediction and red dots represent the points removed from each realization.

- [6] Shoufa Chen, Peize Sun, Yibing Song, and Ping Luo. Diffusiondet: Diffusion model for object detection. *arXiv preprint arXiv:2211.09788*, 2022.
- [7] Zhi-Qi Cheng, Qi Dai, Hong Li, Jingkuan Song, Xiao Wu, and Alexander G Hauptmann. Rethinking spatial invariance of convolutional networks for object counting. In *Proceedings of the IEEE/CVF Conference on Computer Vision and Pattern Recognition*, pages 19638–19648, 2022.
- [8] Jooyoung Choi, Jungbeom Lee, Chaehun Shin, Sungwon Kim, Hyunwoo Kim, and Sungroh Yoon. Percep-

- tion prioritized training of diffusion models. In *Proceedings of the IEEE/CVF Conference on Computer Vision and Pattern Recognition*, pages 11472–11481, 2022.
- [9] Kamil Deja, Tomasz Trzcinski, and Jakub M Tomczak. Learning data representations with joint diffusion models. *arXiv preprint arXiv:2301.13622*, 2023.
- [10] Guoxiu Duan, Aichun Zhu, Lu Zhao, Xiaomei Zhu, Fangqiang Hu, and Xinjie Guan. Mask-based generative adversarial networking for crowd counting. *Journal of Electronic Imaging*, 30(4):043027–043027,

2021.

- [11] Hui Gao, Wenjun Zhao, Dexian Zhang, and Miaolei Deng. Application of improved transformer based on weakly supervised in crowd localization and crowd counting. *Scientific Reports*, 13(1):1144, 2023.
- [12] Zhangxuan Gu, Haoxing Chen, Zhuoer Xu, Jun Lan, Changhua Meng, and Weiqiang Wang. Diffusion-inst: Diffusion model for instance segmentation. *arXiv* preprint arXiv:2212.02773, 2022.
- [13] Jonathan Ho, Ajay Jain, and Pieter Abbeel. Denoising diffusion probabilistic models. *Advances in Neural Information Processing Systems*, 33:6840–6851, 2020.
- [14] Yutao Hu, Xiaolong Jiang, Xuhui Liu, Baochang Zhang, Jungong Han, Xianbin Cao, and David Doermann. Nas-count: Counting-by-density with neural architecture search. In Computer Vision–ECCV 2020: 16th European Conference, Glasgow, UK, August 23– 28, 2020, Proceedings, Part XXII 16, pages 747–766. Springer, 2020.
- [15] Haroon Idrees, Imran Saleemi, Cody Seibert, and Mubarak Shah. Multi-source multi-scale counting in extremely dense crowd images. In *Proceedings of the IEEE conference on computer vision and pattern recognition*, pages 2547–2554, 2013.
- [16] Haroon Idrees, Muhmmad Tayyab, Kishan Athrey, Dong Zhang, Somaya Al-Maadeed, Nasir Rajpoot, and Mubarak Shah. Composition loss for counting, density map estimation and localization in dense crowds. In *Proceedings of the European conference* on computer vision (ECCV), pages 532–546, 2018.
- [17] Xiaoheng Jiang, Li Zhang, Mingliang Xu, Tianzhu Zhang, Pei Lv, Bing Zhou, Xin Yang, and Yanwei Pang. Attention scaling for crowd counting. In *Proceedings of the IEEE/CVF conference on computer vision and pattern recognition*, pages 4706–4715, 2020.
- [18] Haoying Li, Yifan Yang, Meng Chang, Shiqi Chen, Huajun Feng, Zhihai Xu, Qi Li, and Yueting Chen. Srdiff: Single image super-resolution with diffusion probabilistic models. *Neurocomputing*, 479:47–59, 2022.
- [19] Yuhong Li, Xiaofan Zhang, and Deming Chen. Csrnet: Dilated convolutional neural networks for understanding the highly congested scenes. In *Proceedings of the IEEE conference on computer vision and pattern recognition*, pages 1091–1100, 2018.
- [20] Dongze Lian, Jing Li, Jia Zheng, Weixin Luo, and Shenghua Gao. Density map regression guided detection network for rgb-d crowd counting and localization. In *Proceedings of the IEEE/CVF Conference* on Computer Vision and Pattern Recognition, pages 1821–1830, 2019.

- [21] Dingkang Liang, Xiwu Chen, Wei Xu, Yu Zhou, and Xiang Bai. Transcrowd: weakly-supervised crowd counting with transformers. *Science China Information Sciences*, 65(6):160104, 2022.
- [22] Dingkang Liang, Wei Xu, and Xiang Bai. An end-to-end transformer model for crowd localization. In Computer Vision–ECCV 2022: 17th European Conference, Tel Aviv, Israel, October 23–27, 2022, Proceedings, Part I, pages 38–54. Springer, 2022.
- [23] Dingkang Liang, Wei Xu, Yingying Zhu, and Yu Zhou. Focal inverse distance transform maps for crowd localization. *IEEE Transactions on Multime*dia, 2022.
- [24] Hui Lin, Zhiheng Ma, Rongrong Ji, Yaowei Wang, and Xiaopeng Hong. Boosting crowd counting via multifaceted attention. In *Proceedings of the IEEE/CVF Conference on Computer Vision and Pattern Recognition*, pages 19628–19637, 2022.
- [25] Liang Liu, Hao Lu, Haipeng Xiong, Ke Xian, Zhiguo Cao, and Chunhua Shen. Counting objects by blockwise classification. *IEEE Transactions on Circuits and Systems for Video Technology*, 30(10):3513–3527, 2019.
- [26] Liang Liu, Hao Lu, Hongwei Zou, Haipeng Xiong, Zhiguo Cao, and Chunhua Shen. Weighing counts: Sequential crowd counting by reinforcement learning. In Computer Vision–ECCV 2020: 16th European Conference, Glasgow, UK, August 23–28, 2020, Proceedings, Part X 16, pages 164–181. Springer, 2020.
- [27] Weizhe Liu, Mathieu Salzmann, and Pascal Fua. Context-aware crowd counting. In Proceedings of the IEEE/CVF conference on computer vision and pattern recognition, pages 5099–5108, 2019.
- [28] Xiyang Liu, Jie Yang, Wenrui Ding, Tieqiang Wang, Zhijin Wang, and Junjun Xiong. Adaptive mixture regression network with local counting map for crowd counting. In Computer Vision–ECCV 2020: 16th European Conference, Glasgow, UK, August 23–28, 2020, Proceedings, Part XXIV 16, pages 241–257. Springer, 2020.
- [29] Yuting Liu, Miaojing Shi, Qijun Zhao, and Xiaofang Wang. Point in, box out: Beyond counting persons in crowds. In *Proceedings of the IEEE/CVF Conference on Computer Vision and Pattern Recognition*, pages 6469–6478, 2019.
- [30] Ao Luo, Fan Yang, Xin Li, Dong Nie, Zhicheng Jiao, Shangchen Zhou, and Hong Cheng. Hybrid graph neural networks for crowd counting. In *Proceedings of the AAAI conference on artificial intelligence*, volume 34, pages 11693–11700, 2020.

- [31] Zhiheng Ma, Xing Wei, Xiaopeng Hong, Hui Lin, Yunfeng Qiu, and Yihong Gong. Learning to count via unbalanced optimal transport. In *Proceedings of the AAAI Conference on Artificial Intelligence*, volume 35, pages 2319–2327, 2021.
- [32] Yanda Meng, Hongrun Zhang, Yitian Zhao, Xiaoyun Yang, Xuesheng Qian, Xiaowei Huang, and Yalin Zheng. Spatial uncertainty-aware semi-supervised crowd counting. In *Proceedings of the IEEE/CVF International Conference on Computer Vision*, pages 15549–15559, 2021.
- [33] Yunqi Miao, Zijia Lin, Guiguang Ding, and Jungong Han. Shallow feature based dense attention network for crowd counting. In *Proceedings of the AAAI conference on artificial intelligence*, volume 34, pages 11765–11772, 2020.
- [34] Alexander Quinn Nichol and Prafulla Dhariwal. Improved denoising diffusion probabilistic models. In *International Conference on Machine Learning*, pages 8162–8171. PMLR, 2021.
- [35] Min-hwan Oh, Peder Olsen, and Karthikeyan Natesan Ramamurthy. Crowd counting with decomposed uncertainty. In *Proceedings of the AAAI conference on artificial intelligence*, volume 34, pages 11799–11806, 2020.
- [36] Robin Rombach, Andreas Blattmann, Dominik Lorenz, Patrick Esser, and Björn Ommer. Highresolution image synthesis with latent diffusion models. In *Proceedings of the IEEE/CVF Conference* on Computer Vision and Pattern Recognition, pages 10684–10695, 2022.
- [37] Deepak Babu Sam, Skand Vishwanath Peri, Mukuntha Narayanan Sundararaman, Amogh Kamath, and R Venkatesh Babu. Locate, size, and count: accurately resolving people in dense crowds via detection. *IEEE transactions on pattern analysis and machine intelligence*, 43(8):2739–2751, 2020.
- [38] Jing Shao, Chen Change Loy, and Xiaogang Wang. Scene-independent group profiling in crowd. In *Proceedings of the IEEE conference on computer vision and pattern recognition*, pages 2219–2226, 2014.
- [39] Jing Shao, Kai Kang, Chen Change Loy, and Xiaogang Wang. Deeply learned attributes for crowded scene understanding. In *Proceedings of the IEEE conference on computer vision and pattern recognition*, pages 4657–4666, 2015.
- [40] Zan Shen, Yi Xu, Bingbing Ni, Minsi Wang, Jianguo Hu, and Xiaokang Yang. Crowd counting via adversarial cross-scale consistency pursuit. In *Proceedings* of the IEEE conference on computer vision and pattern recognition, pages 5245–5254, 2018.

- [41] Weibo Shu, Jia Wan, Kay Chen Tan, Sam Kwong, and Antoni B Chan. Crowd counting in the frequency domain. In Proceedings of the IEEE/CVF Conference on Computer Vision and Pattern Recognition, pages 19618–19627, 2022.
- [42] Vishwanath A Sindagi, Rajeev Yasarla, and Vishal M Patel. Pushing the frontiers of unconstrained crowd counting: New dataset and benchmark method. In *Proceedings of the IEEE International Conference on Computer Vision*, pages 1221–1231, 2019.
- [43] Jascha Sohl-Dickstein, Eric Weiss, Niru Maheswaranathan, and Surya Ganguli. Deep unsupervised learning using nonequilibrium thermodynamics. In *In*ternational Conference on Machine Learning, pages 2256–2265. PMLR, 2015.
- [44] Jiaming Song, Chenlin Meng, and Stefano Ermon. Denoising diffusion implicit models. *arXiv preprint arXiv:2010.02502*, 2020.
- [45] Qingyu Song, Changan Wang, Zhengkai Jiang, Yabiao Wang, Ying Tai, Chengjie Wang, Jilin Li, Feiyue Huang, and Yang Wu. Rethinking counting and localization in crowds: A purely point-based framework. In *Proceedings of the IEEE/CVF International Conference on Computer Vision*, pages 3365–3374, 2021.
- [46] Qingyu Song, Changan Wang, Yabiao Wang, Ying Tai, Chengjie Wang, Jilin Li, Jian Wu, and Jiayi Ma. To choose or to fuse? scale selection for crowd counting. In *Proceedings of the AAAI conference on artificial intelligence*, volume 35, pages 2576–2583, 2021.
- [47] Ye Tian, Xiangxiang Chu, and Hongpeng Wang. Cctrans: Simplifying and improving crowd counting with transformer. *arXiv preprint arXiv:2109.14483*, 2021.
- [48] Jia Wan and Antoni Chan. Adaptive density map generation for crowd counting. In *Proceedings of the IEEE/CVF international conference on computer vision*, pages 1130–1139, 2019.
- [49] Jia Wan, Qingzhong Wang, and Antoni B Chan. Kernel-based density map generation for dense object counting. *IEEE Transactions on Pattern Analysis and Machine Intelligence*, 44(3):1357–1370, 2020.
- [50] Boyu Wang, Huidong Liu, Dimitris Samaras, and Minh Hoai Nguyen. Distribution matching for crowd counting. *Advances in neural information processing systems*, 33:1595–1607, 2020.
- [51] Qi Wang, Junyu Gao, Wei Lin, and Yuan Yuan. Learning from synthetic data for crowd counting in the wild. In *Proceedings of the IEEE/CVF conference on computer vision and pattern recognition*, pages 8198–8207, 2019.

- [52] Zhou Wang, Alan C Bovik, Hamid R Sheikh, and Eero P Simoncelli. Image quality assessment: from error visibility to structural similarity. *IEEE transactions on image processing*, 13(4):600–612, 2004.
- [53] Haipeng Xiong, Hao Lu, Chengxin Liu, Liang Liu, Zhiguo Cao, and Chunhua Shen. From open set to closed set: Counting objects by spatial divide-andconquer. In *Proceedings of the IEEE/CVF Interna*tional Conference on Computer Vision, pages 8362– 8371, 2019.
- [54] Chenfeng Xu, Dingkang Liang, Yongchao Xu, Song Bai, Wei Zhan, Xiang Bai, and Masayoshi Tomizuka. Autoscale: learning to scale for crowd counting. *International Journal of Computer Vision*, 130(2):405–434, 2022.
- [55] Hai-Yan Yao, Wang-Gen Wan, and Xiang Li. Mask guided gan for density estimation and crowd counting. *IEEE Access*, 8:31432–31443, 2020.
- [56] Anran Zhang, Lei Yue, Jiayi Shen, Fan Zhu, Xiantong Zhen, Xianbin Cao, and Ling Shao. Attentional neural fields for crowd counting. In *Proceedings of the IEEE/CVF international conference on computer vi*sion, pages 5714–5723, 2019.
- [57] Yingying Zhang, Desen Zhou, Siqin Chen, Shenghua Gao, and Yi Ma. Single-image crowd counting via multi-column convolutional neural network. In *Proceedings of the IEEE conference on computer vision and pattern recognition*, pages 589–597, 2016.
- [58] Xiaopin Zhong, Guankun Wang, Weixiang Liua, Zongze Wua, and Yuanlong Deng. Mask focal loss for dense crowd counting with canonical object detection networks. *arXiv* preprint arXiv:2212.11542, 2022.

### A. Video demonstrations

The following links contain video demonstrations of density map generation as a denoising diffusion process. The density maps are overlayed on the crowd image and we only consider a single realization in the videos. We recommend to download the videos for better quality.

- ShanghaiTech A video demo .avi .mp4
- JHU-CROWD++ video demo 1 .avi .mp4
- JHU-CROWD++ video demo 2 .avi .mp4
- UCF-QNRF video demo .avi .mp4

### **B.** Evaluation metrics

To evaluate crowd-counting performance, we use the mean absolute error (MAE):

$$MAE = \frac{1}{N} \sum_{n=1}^{N} \|c_n - \bar{c_n}\|_1,$$
 (9)

and root mean squared error (MSE):

$$MSE = \sqrt{\frac{1}{N} \sum_{n=1}^{N} \|c_n - \bar{c_n}\|_2^2}$$
 (10)

as the performance metrics. Here, N is the total number of test samples,  $c_n$  is the ground truth count, and  $\bar{c_n}$  is the prediction for the  $n^{\text{th}}$  sample.

# C. Datasets

We evaluate our method on five public datasets: JHU-CROWD++ [42], ShanghaiTech A [57], ShanghaiTech B [57], UCF\_CC\_50 [15], and UCF-QNRF [16] for crowd counting.

**JHU-CROWD++** has 2,722 training images, 500 validation images, and 1,600 test images, collected from diverse scenarios. The dataset consists of crowd images with numbers ranging up to 25,791 and images without any crowd.

**ShanghaiTech A** contains 300 training images and 182 test images with annotations. We randomly select 30 samples from the training dataset as the validation dataset.

**ShanghaiTech B** contains 400 training images and 316 testing images with annotations. We create a validation dataset with randomly selected 40 crowd images from the training dataset.

UCF\_CC\_50 is a comparatively small crowd dataset for extremely dense crowd counting with just 50 samples. We perform a 5-fold cross-validation following the standard protocol in [15].

**UCF-QNRF** dataset contains 1,535 images of unconstrained crowd scenes, with approximately one million annotations in total. The dataset is split into a training set of 1,201 images and a testing set of 334 images, and we create a validation set of 60 images.

#### D. Pseudocodes

The pseudocode for training is given in Algorithm 1 and testing in Algorithm 2.

#### E. Performance for individual realizations

In Table 5 we provide the counting performance for each of the four realizations used in the final crowd counting prediction with and without the counting decoder.

	Method	JHU-CR	JHU-CROWD++		aiTech B	UCF-QNRF	
	Method	MAE↓	MSE↓	MAE↓	MSE↓	MAE↓	MSE↓
	Trial 1	54.23	219.76	6.31	10.00	72.39	131.98
	Trial 2	56.11	225.24	6.25	9.91	75.52	134.33
0	Trial 3	55.91	224.65	6.47	10.25	73.67	132.09
w/o	Trial 4	52.56	215.01	6.28	9.95	77.44	136.71
	Average	54.70	221.17	6.33	10.03	74.76	133.78
	Variance	1.6586	4.7822	0.0981	0.1528	2.2034	2.2348
	Trial 1	51.11	210.96	6.19	9.79	69.74	129.75
	Trial 2	50.83	209.45	6.17	9.76	70.17	129.97
-	Trial 3	50.78	209.17	6.22	9.86	68.86	128.49
/M	Trial 4	50.46	209.05	6.21	9.82	70.14	129.91
	Average	50.80	209.66	6.20	9.81	69.73	129.53
	Variance	0.2664	0.8844	0.0222	0.0427	0.6106	0.6995

Table 5. Error metrics for individual realizations without (top half) and with (bottom half) the counting decoder.

#### **Algorithm 1** Training phase

```
def train(images, density_maps, gt_counts):
      images: [B, H, W, 3]
      density_maps: [B, H, W]
   gt_counts: [B,]
   # Density scaling
   density_maps = (2 * scale * density_maps - 1)
   # Corrupt density_maps
   t = randint(0, T)
                               # time step
   eps = normal(mean=0, std=1) # noise: [B, H, W]
   crpt_density_maps =
    diffusion_process(density_maps, eps, t)
   # Estimate noise and encoder-decoder features
   eps_pred, feats =
    denoising_network(images, crpt_density_maps, t)
   # Estimate crowd count
   count_est = counting_decoder(feats)
    Compute denoising network loss
    l_hybrid(eps_pred, eps) +
    count_scale * 11_loss(count_est, gt_count)
   return loss
```

### Algorithm 2 Testing phase

```
def testing(images, realizations):
   images: [B, H, W, 3]
realizations: N
    # Encode image features
   feats = image_encoder(images)
   # noisy density maps: [B, H, W]
density_pred = normal(mean=0, std=1)
    # uniform sample step size
   times = reversed(
   linespace(diffusion_steps, sampling_steps))
    # Perform DDIM sampling
   for t in times:
    # Predict noise from density_pred
    eps_hat = denoising_network(images,
       noisy_density, t)
# Compute posterior of noisy density
       density_pred = q_posterior(noisy_density, eps,
    # Detect head locations
   locations = contours(density_pred) # [B, N, *, 2]
    # Perform crowd map fusion: [B, *, 2]
   final_locations = crowd_map_fusion(locations)
   # Compute crowd count
   count_est = count(final_locations) # [B, ]
  return count_est
```

Configuration	setting
Optimizer	Adamw
Optimizer betas	{0.9, 0.999}
Base learning rate	1e-4
Warmup steps	5000
Training steps	2e5
Image size	$256 \times 256$
Batch size	8
Diffusion steps	1000
Noise schedule	Linear

Table 6. Training parameters for the crowd counting network

# F. Training setting

The training parameters used for the denoising network and the counting decoder are presented in Table 6.

# G. Additional qualitative results

Here we provide more qualitative results for the proposed crowd-counting pipeline. The ground truth crowd map, the final prediction along with individual trials are provided for labeled data. In each individual trial, the accepted points and rejected points are illustrated on the image.

Furthermore, we have provided more visual results for density maps and crowd maps for **unlabeled data**. *Density maps are best viewed in the highest zoom level*.

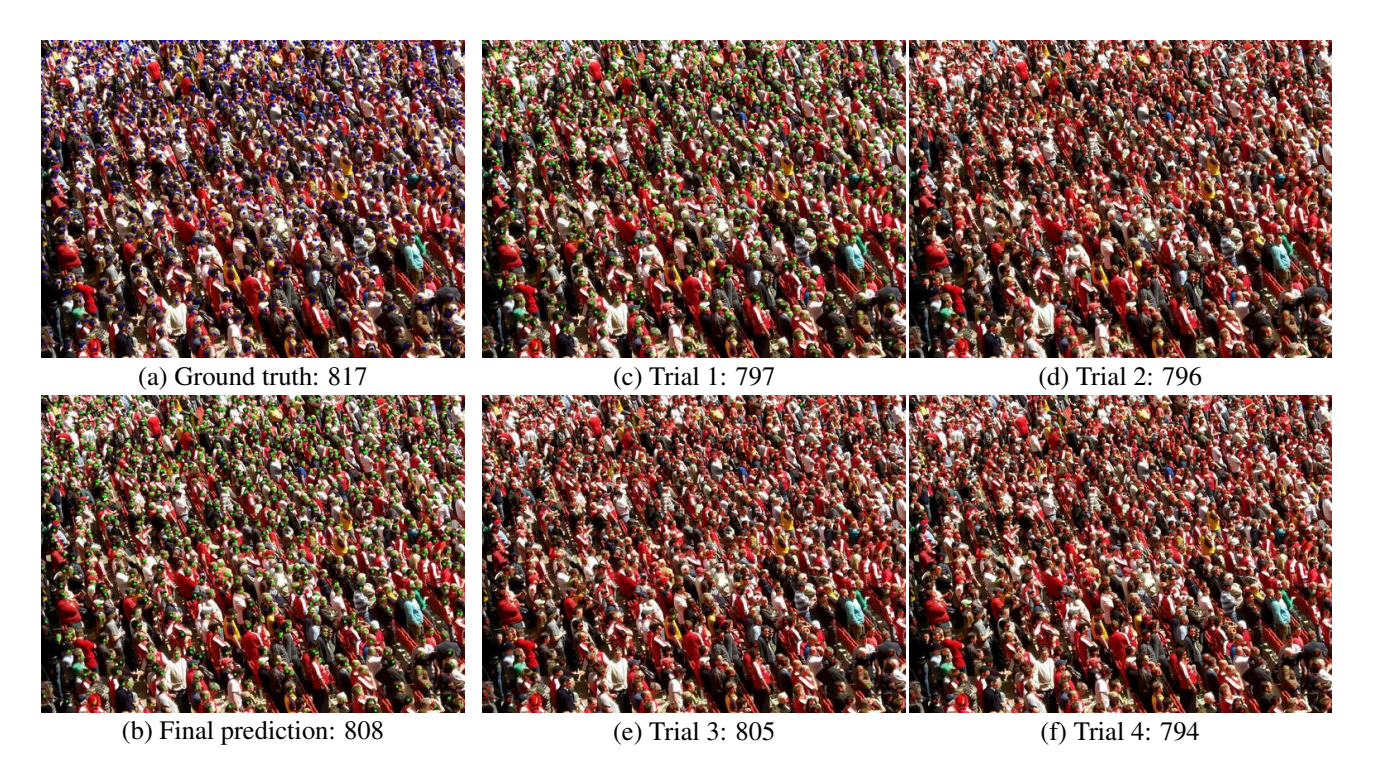


Figure 11. Additional qualitative results for stochastic generation and crowd map fusion. The green dots in each individual trial represent the points included for the final prediction and the red dots are the rejected points.

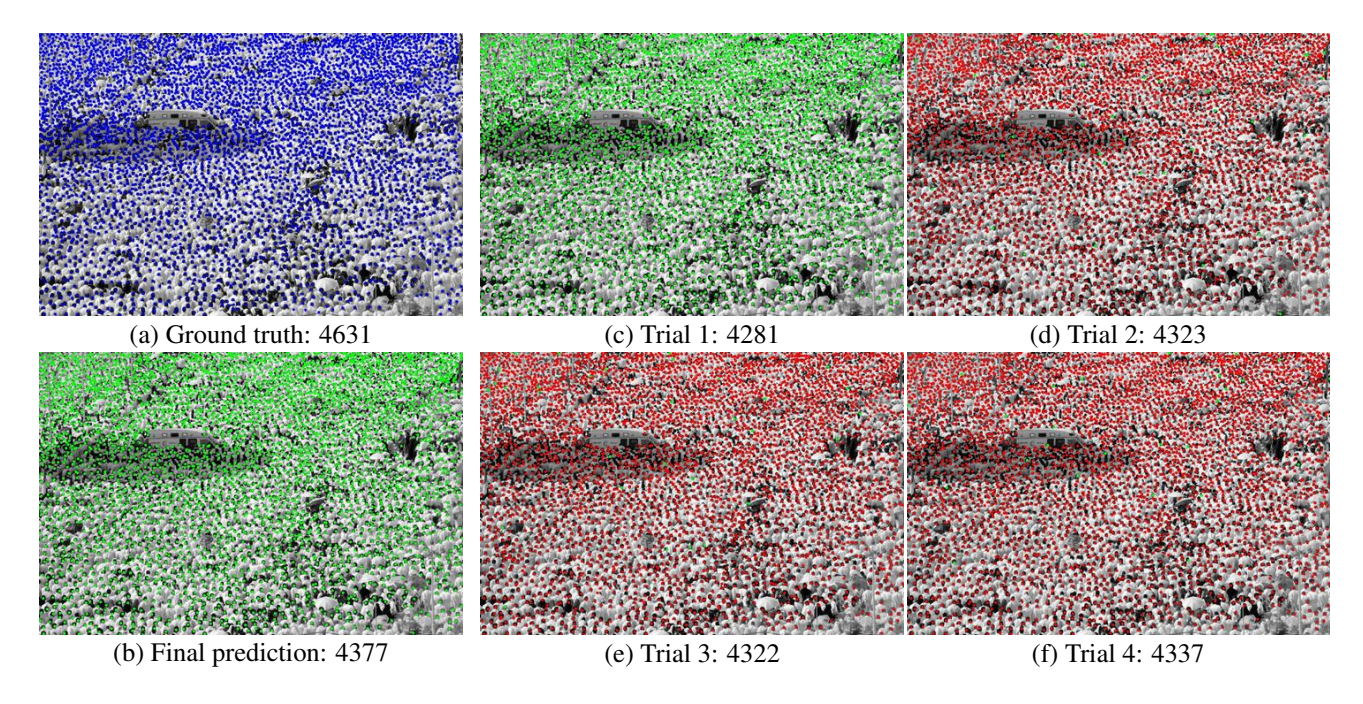


Figure 12. Additional qualitative results for stochastic generation and crowd map fusion. The green dots in each individual trial represent the points included for the final prediction and the red dots are the rejected points.

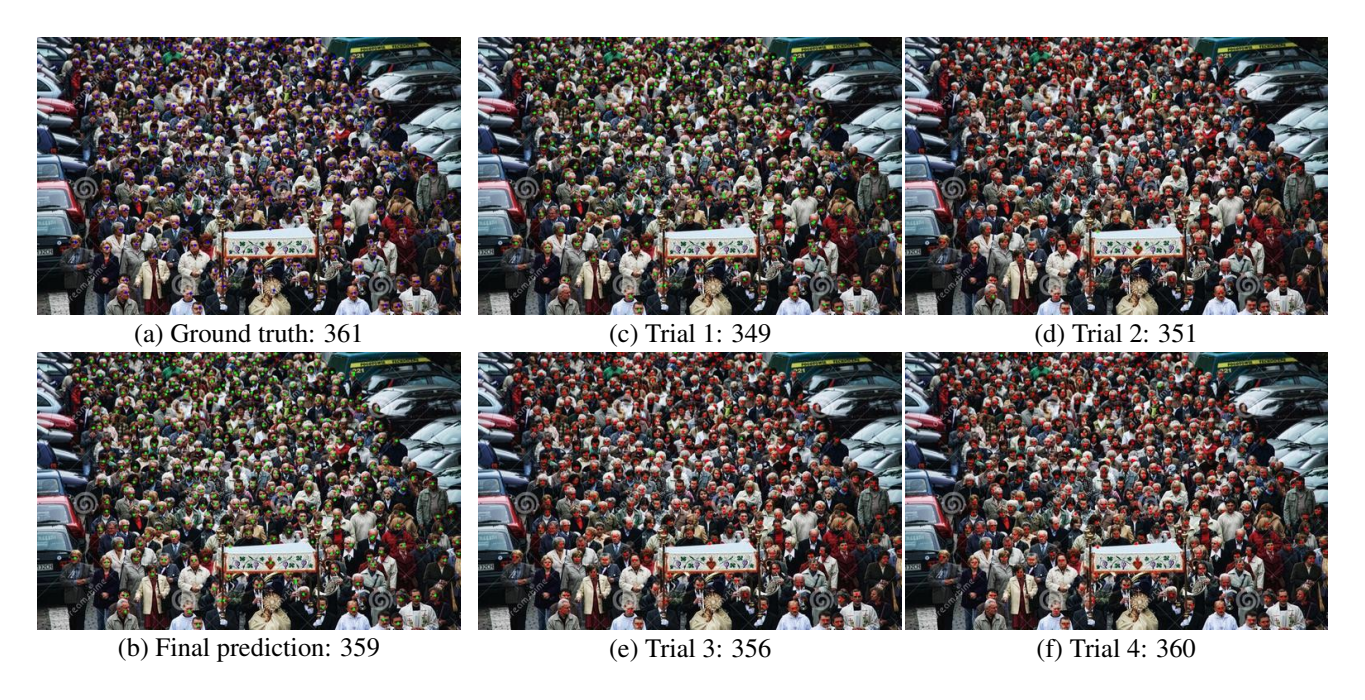


Figure 13. Additional qualitative results for stochastic generation and crowd map fusion. The green dots in each individual trial represent the points included for the final prediction and the red dots are the rejected points.

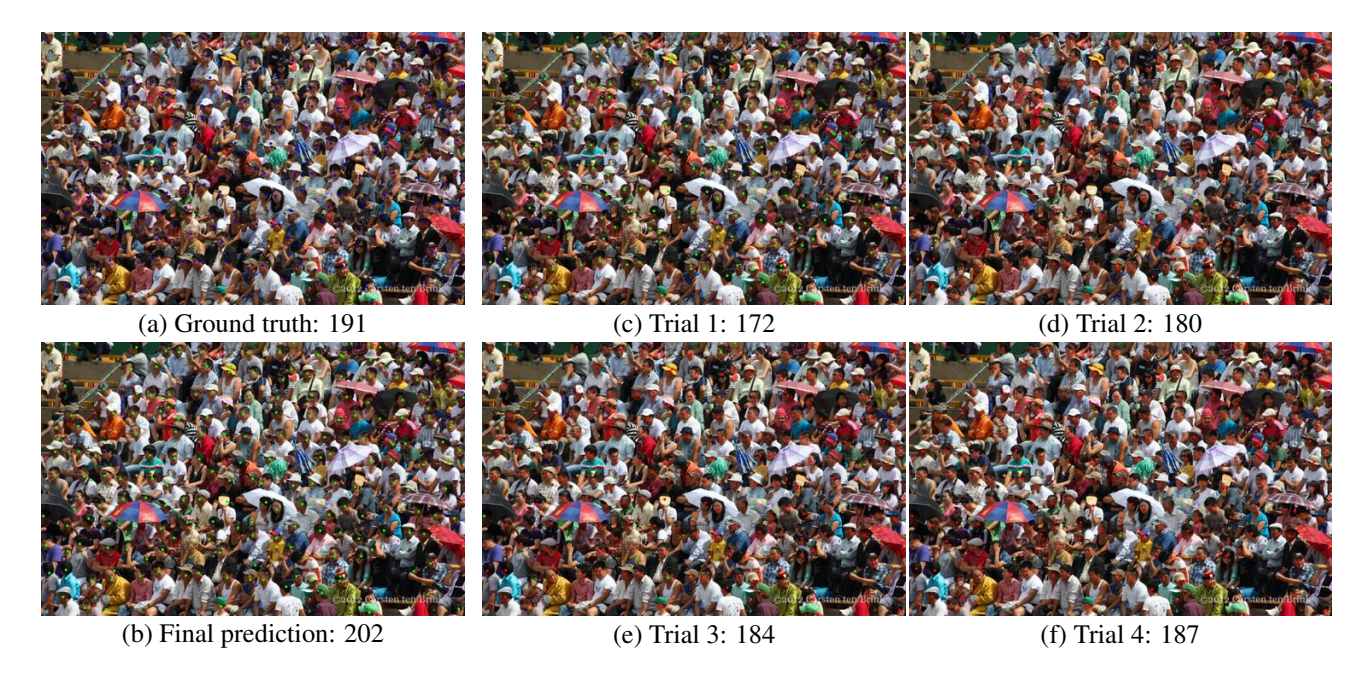


Figure 14. Additional qualitative results for stochastic generation and crowd map fusion. The green dots in each individual trial represent the points included for the final prediction and the red dots are the rejected points.

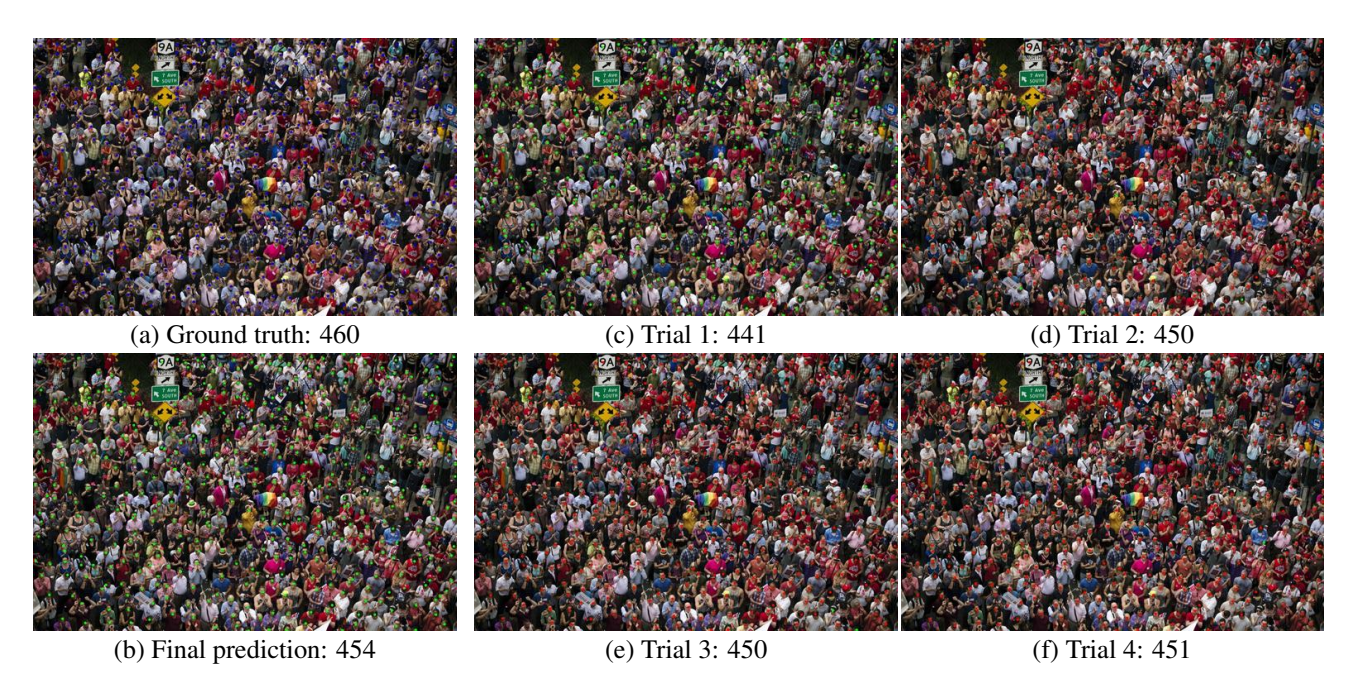


Figure 15. Additional qualitative results for stochastic generation and crowd map fusion. The green dots in each individual trial represent the points included for the final prediction and the red dots are the rejected points.

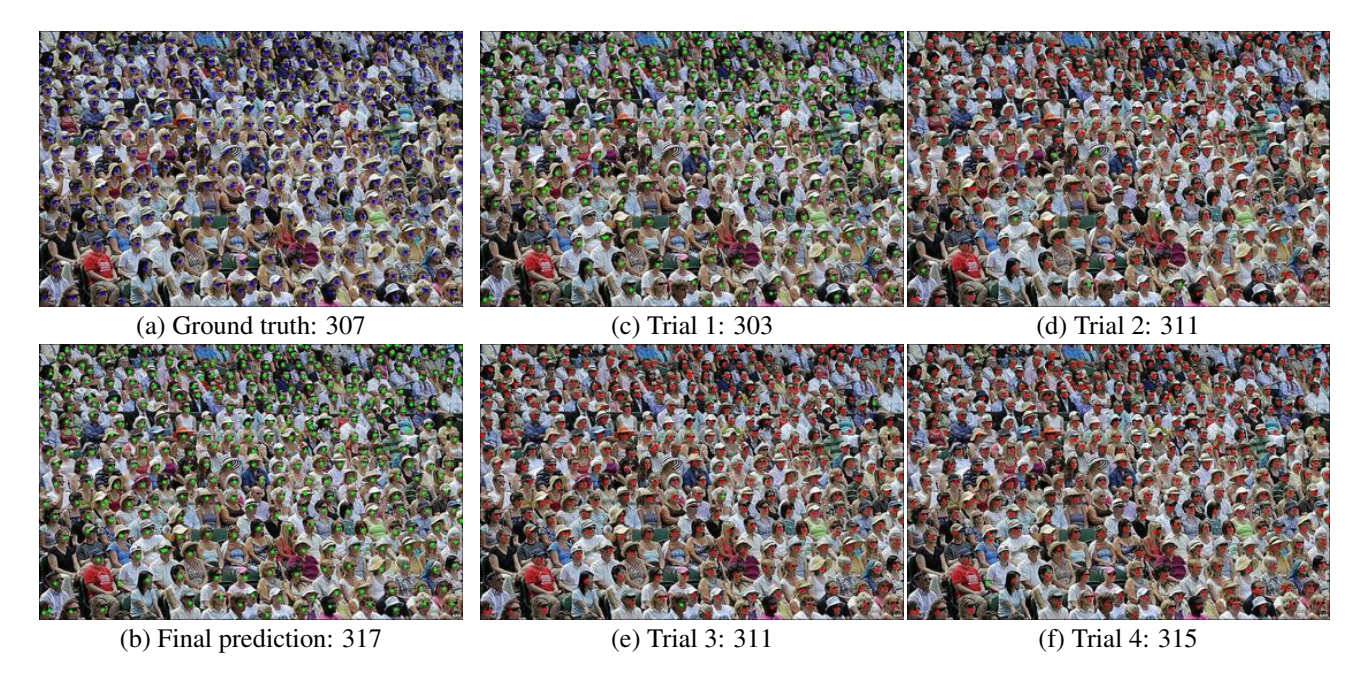


Figure 16. Additional qualitative results for stochastic generation and crowd map fusion. The green dots in each individual trial represent the points included for the final prediction and the red dots are the rejected points.

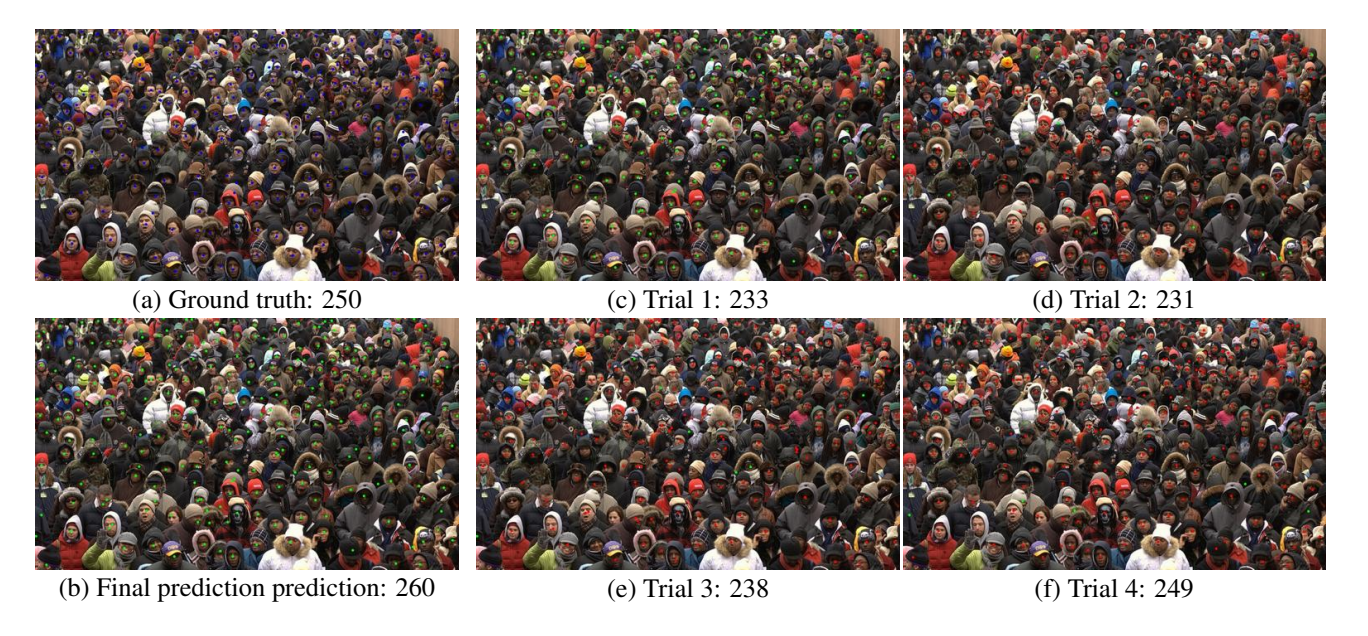


Figure 17. Additional qualitative results for stochastic generation and crowd map fusion. The green dots in each individual trial represent the points included for the final prediction and the red dots are the rejected points.

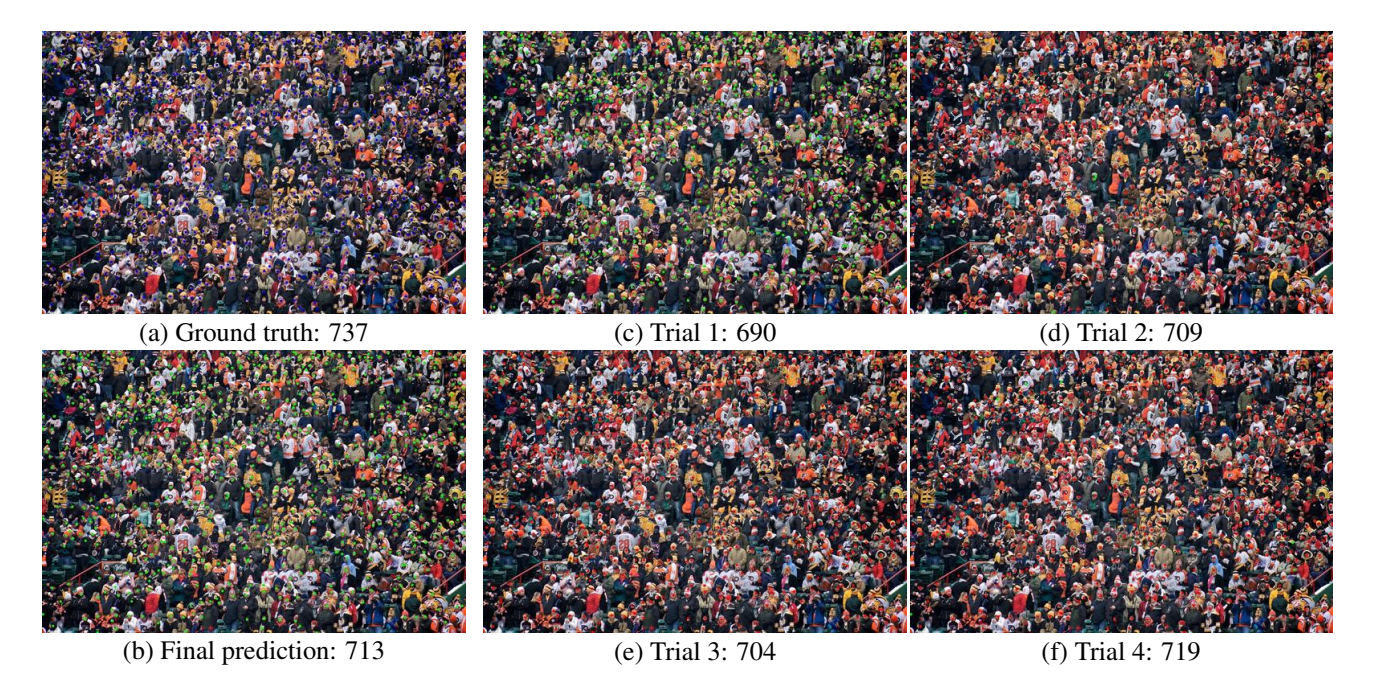


Figure 18. Additional qualitative results for stochastic generation and crowd map fusion. The green dots in each individual trial represent the points included for the final prediction and the red dots are the rejected points.

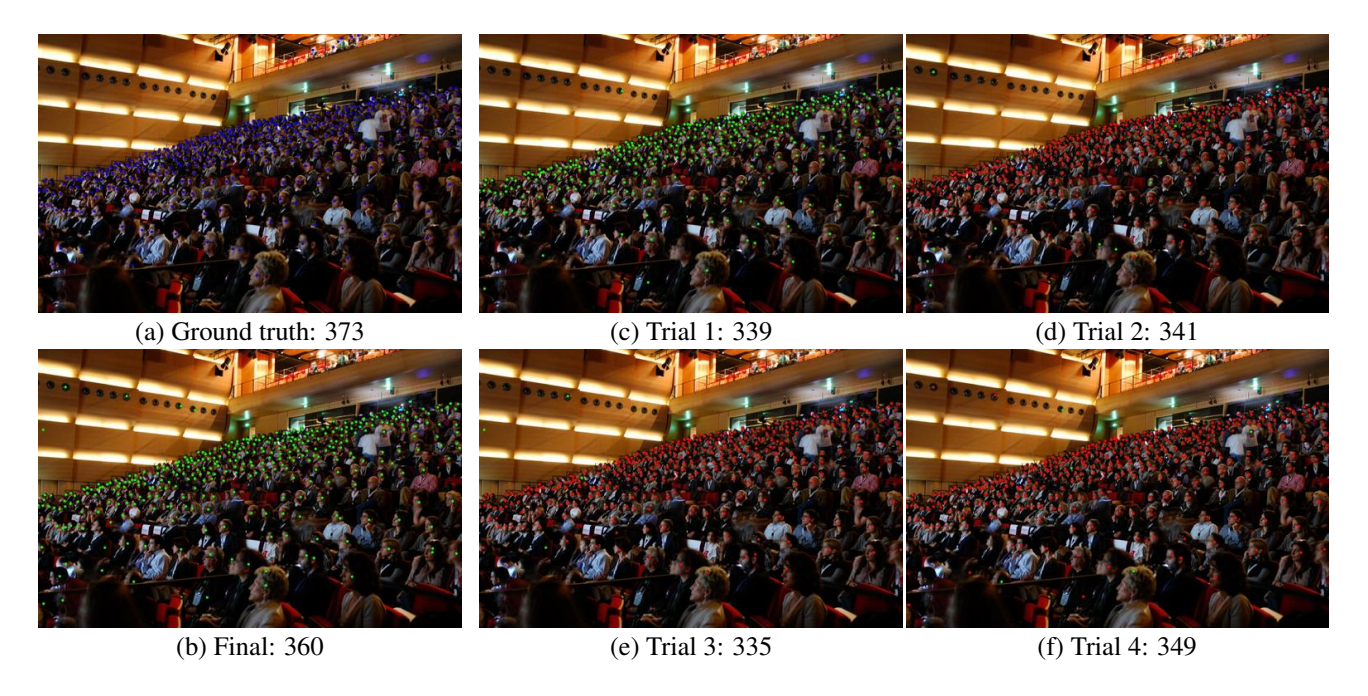


Figure 19. Additional qualitative results for stochastic generation and crowd map fusion.

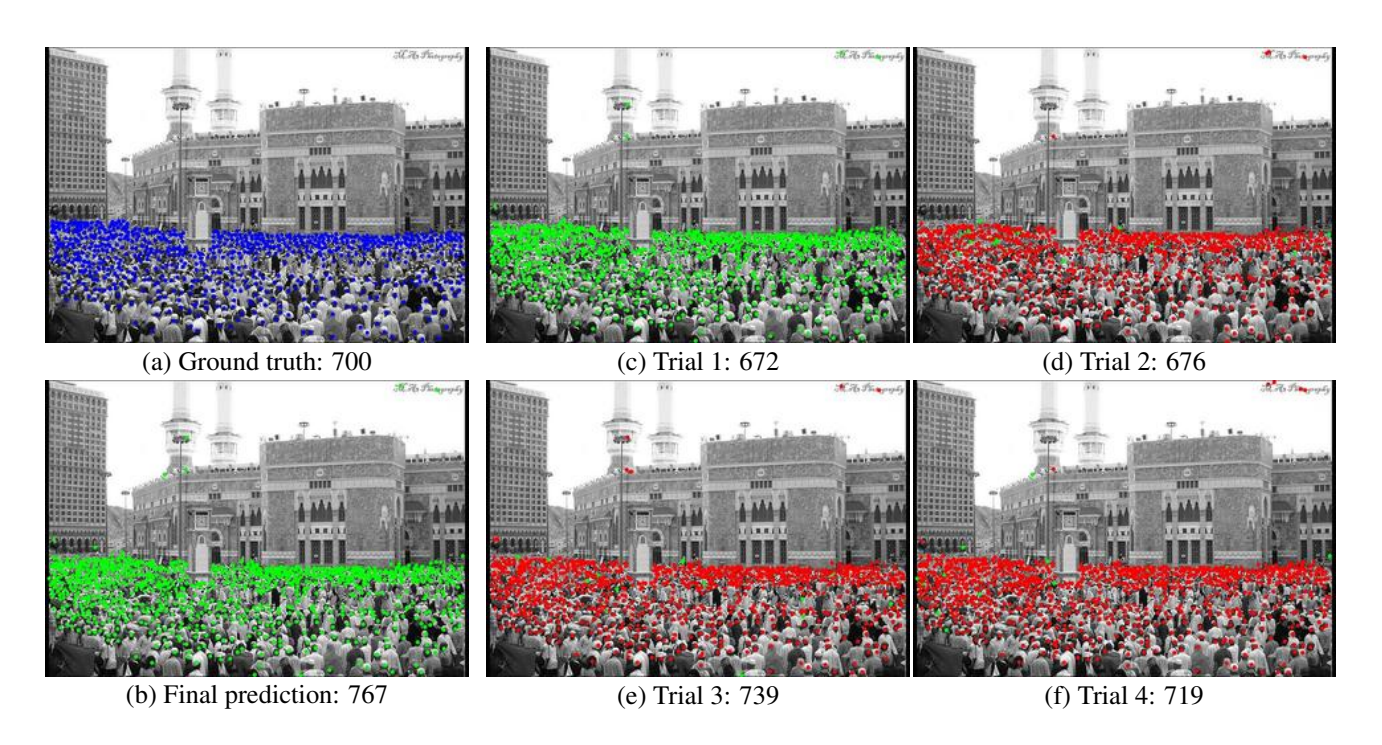


Figure 20. Additional qualitative results for stochastic generation and crowd map fusion. The green dots in each individual trial represent the points included for the final prediction and the red dots are the rejected points.

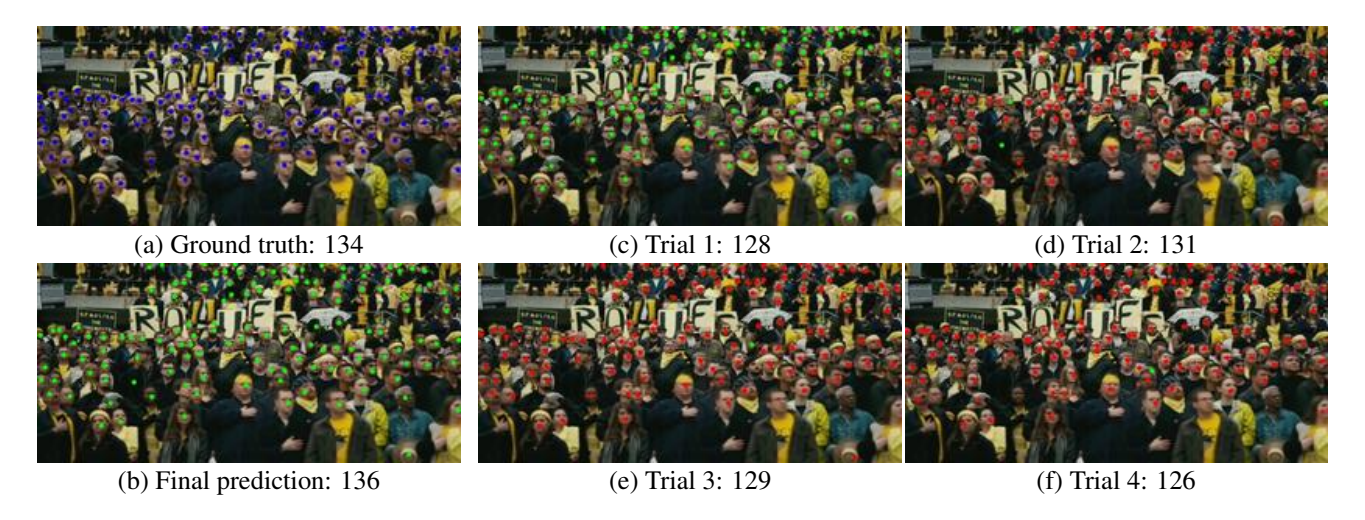


Figure 21. Additional qualitative results for stochastic generation and crowd map fusion. The green dots in each individual trial represent the points included for the final prediction and the red dots are the rejected points.

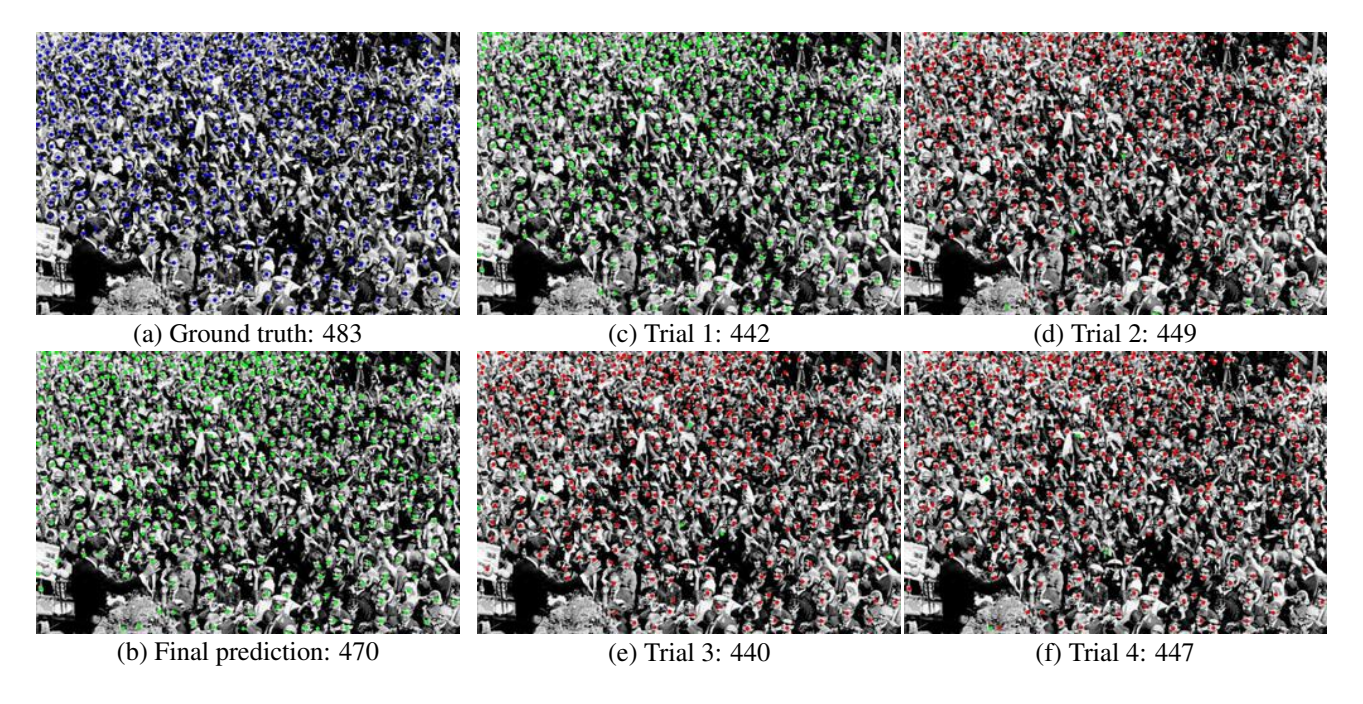


Figure 22. Additional qualitative results for stochastic generation and crowd map fusion. The green dots in each individual trial represent the points included for the final prediction and the red dots are the rejected points.

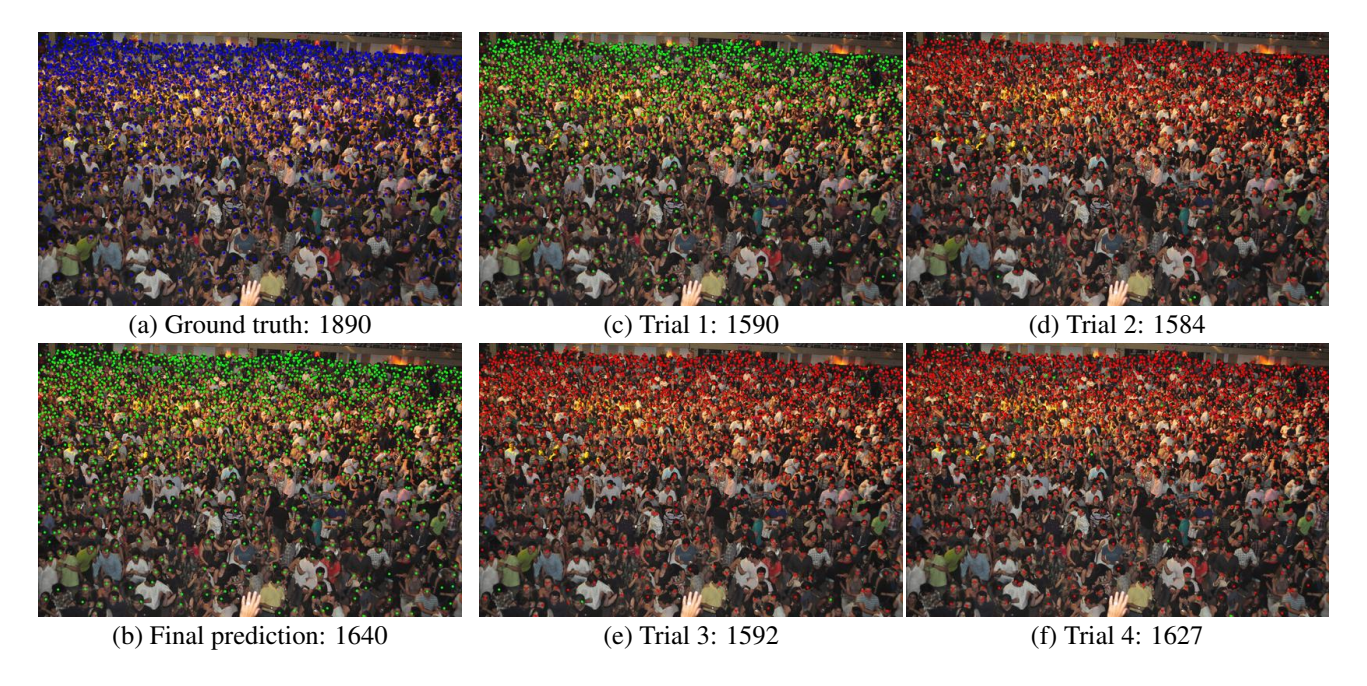


Figure 23. Additional qualitative results for stochastic generation and crowd map fusion. The green dots in each individual trial represent the points included for the final prediction and the red dots are the rejected points.

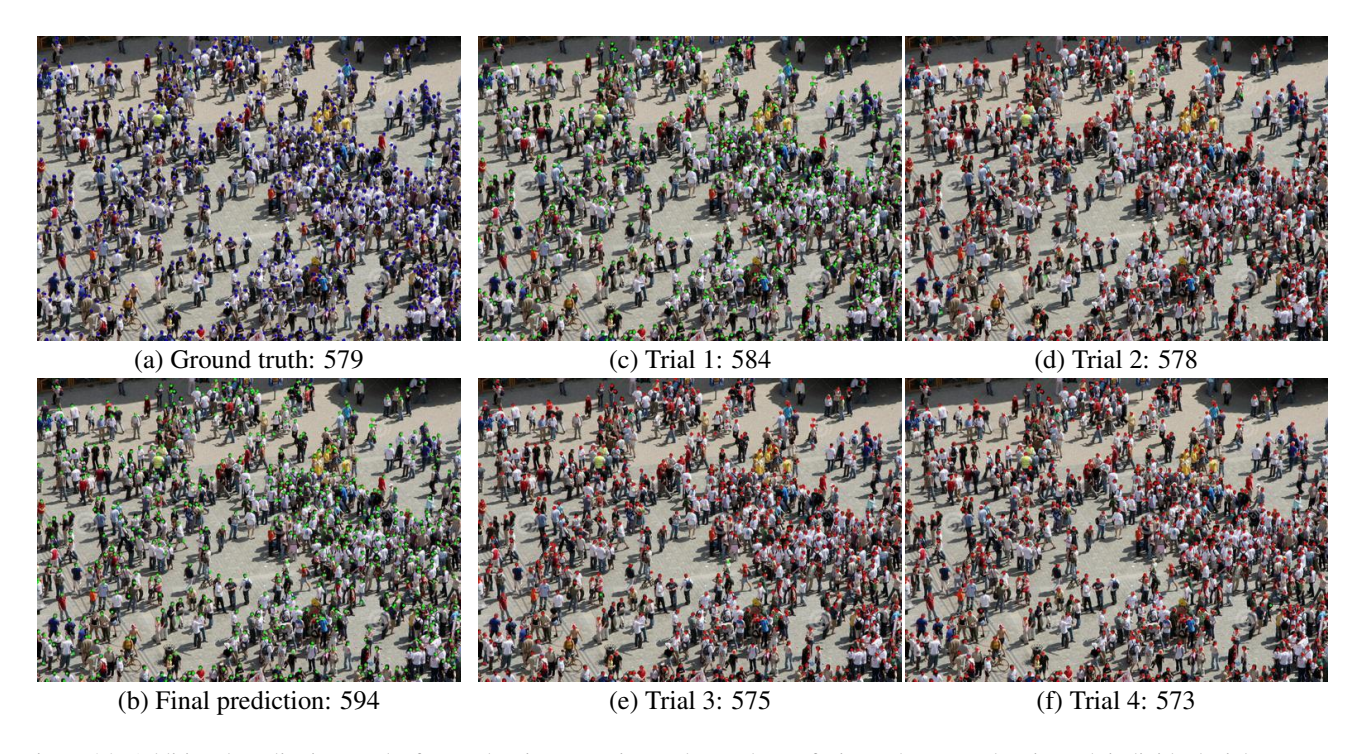


Figure 24. Additional qualitative results for stochastic generation and crowd map fusion. The green dots in each individual trial represent the points included for the final prediction and the red dots are the rejected points.



Figure 25. Additional qualitative results for stochastic generation and crowd map fusion. The green dots in each individual trial represent the points included for the final prediction and the red dots are the rejected points.

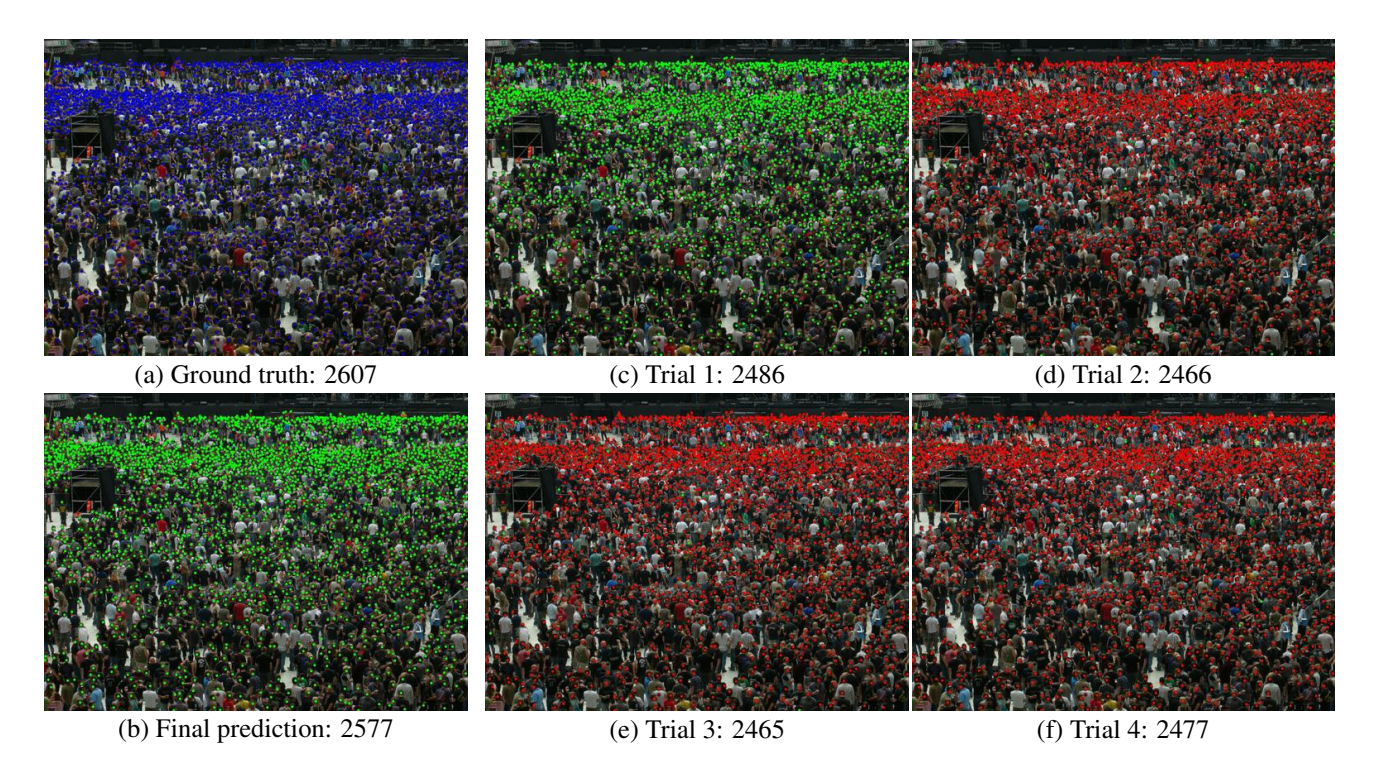


Figure 26. Additional qualitative results for stochastic generation and crowd map fusion. The green dots in each individual trial represent the points included for the final prediction and the red dots are the rejected points.

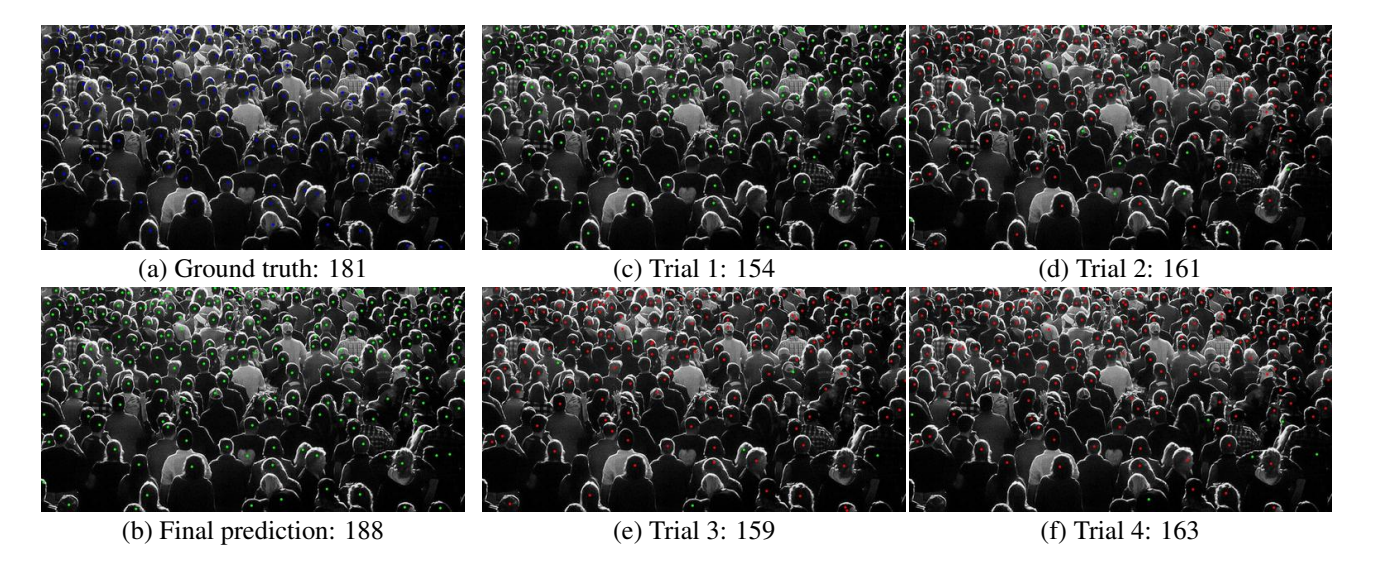


Figure 27. Additional qualitative results for stochastic generation and crowd map fusion. The green dots in each individual trial represent the points included for the final prediction and the red dots are the rejected points.

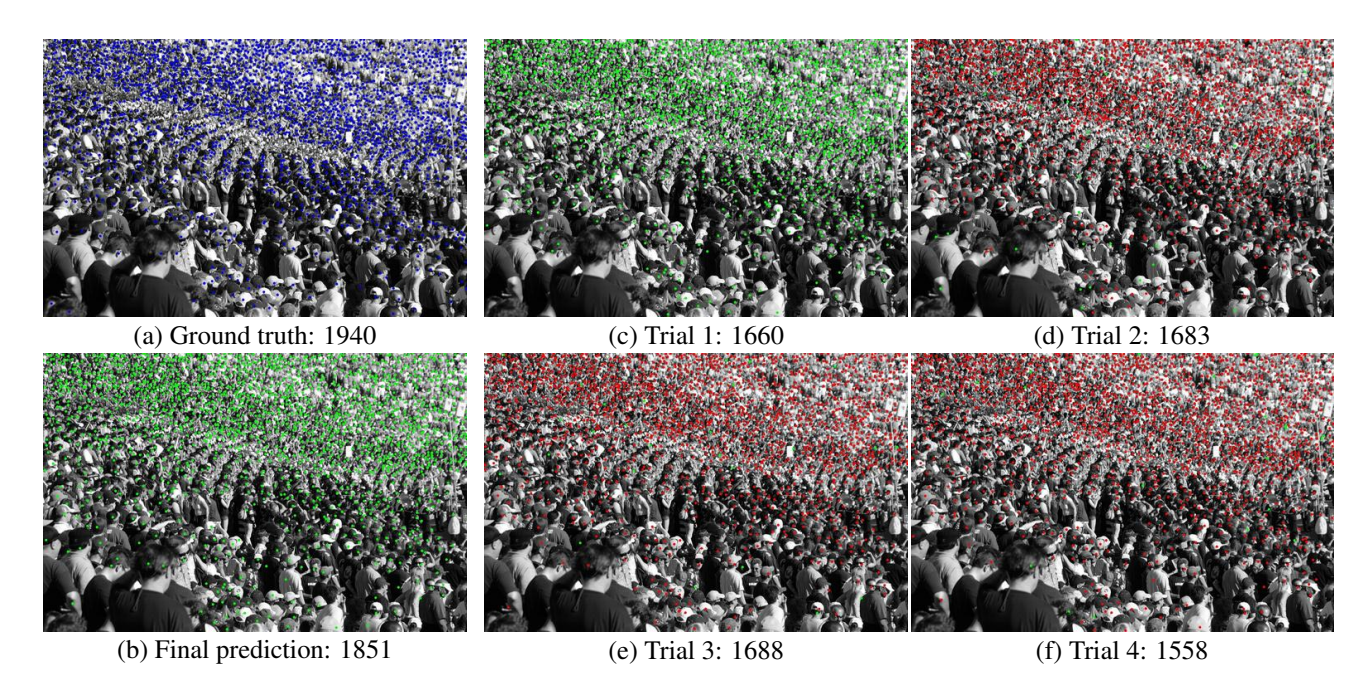


Figure 28. Additional qualitative results for stochastic generation and crowd map fusion. The green dots in each individual trial represent the points included for the final prediction and the red dots are the rejected points.



Figure 29. Additional qualitative results for stochastic generation and crowd map fusion. The green dots in each individual trial represent the points included for the final prediction and the red dots are the rejected points.

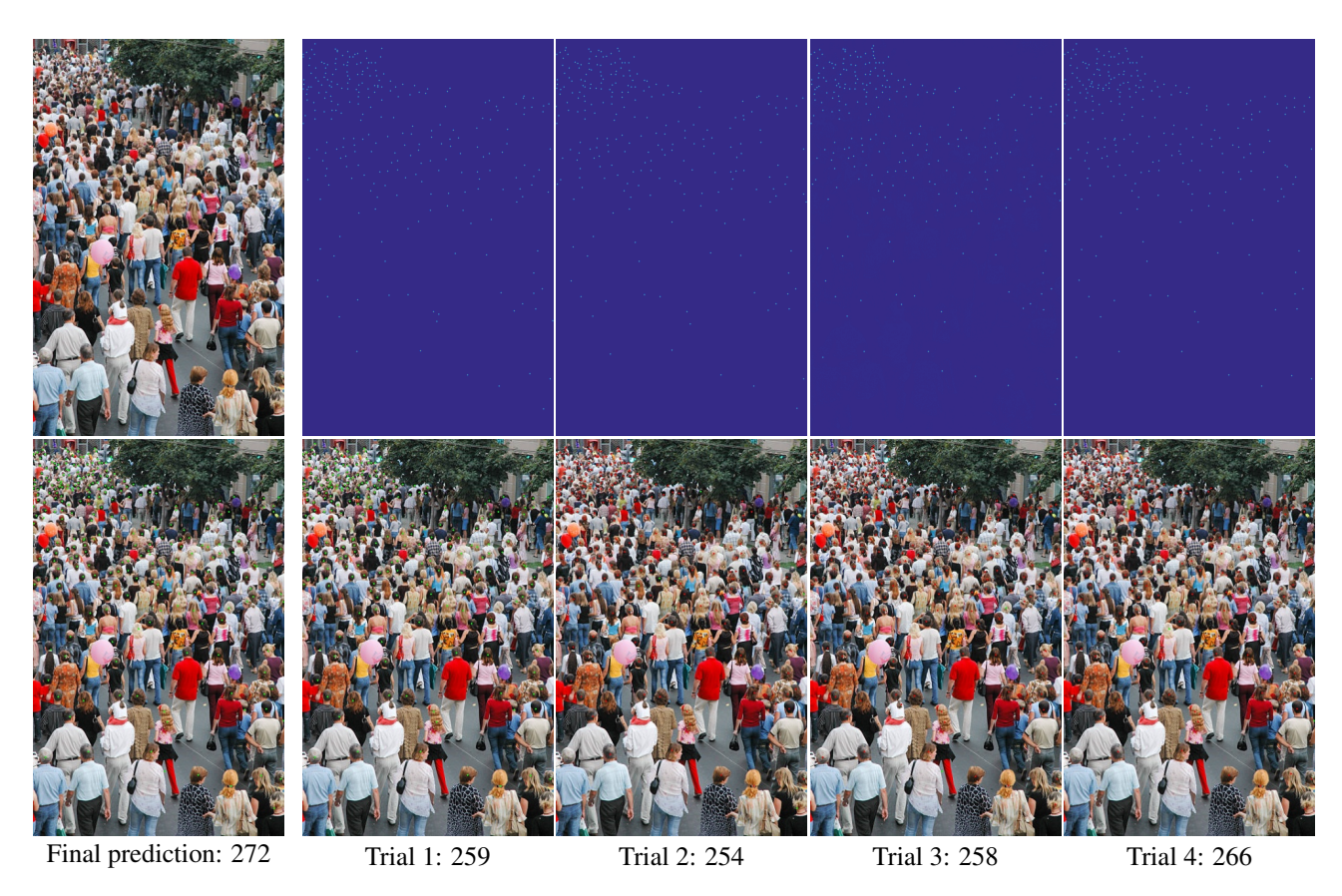


Figure 30. Additional qualitative results for crowd density maps and crowd maps for unlabeled images. The green dots in each individual trial represent the points included for the final prediction and the red dots are the rejected points.

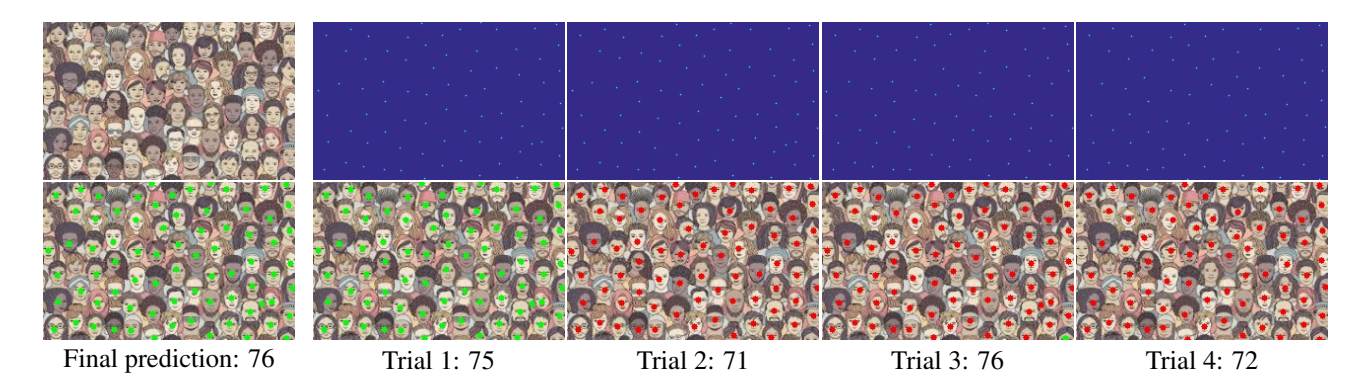


Figure 31. Additional qualitative results for crowd density maps and crowd maps for unlabeled images. The green dots in each individual trial represent the points included for the final prediction and the red dots are the rejected points.

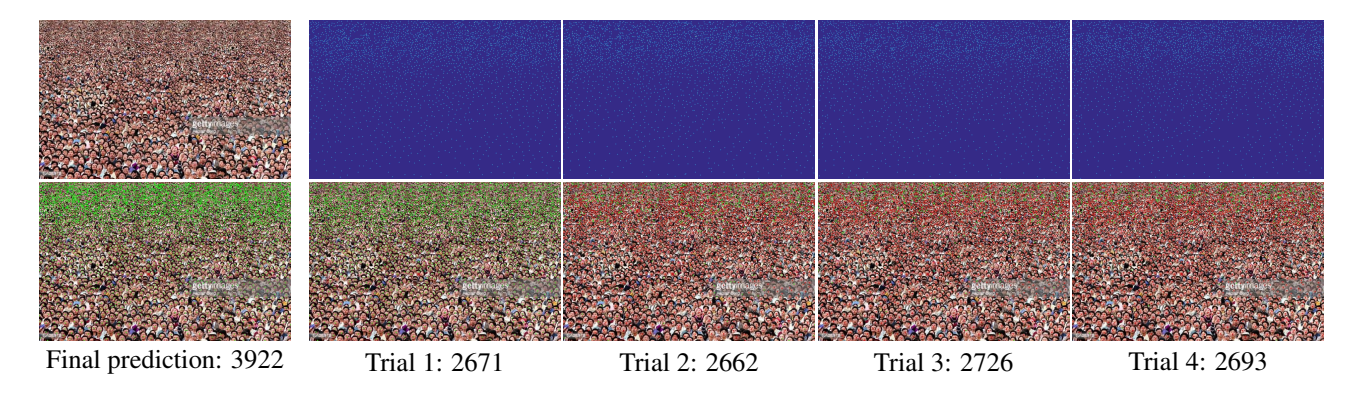


Figure 32. Additional qualitative results for crowd density maps and crowd maps for unlabeled images. The green dots in each individual trial represent the points included for the final prediction and the red dots are the rejected points.

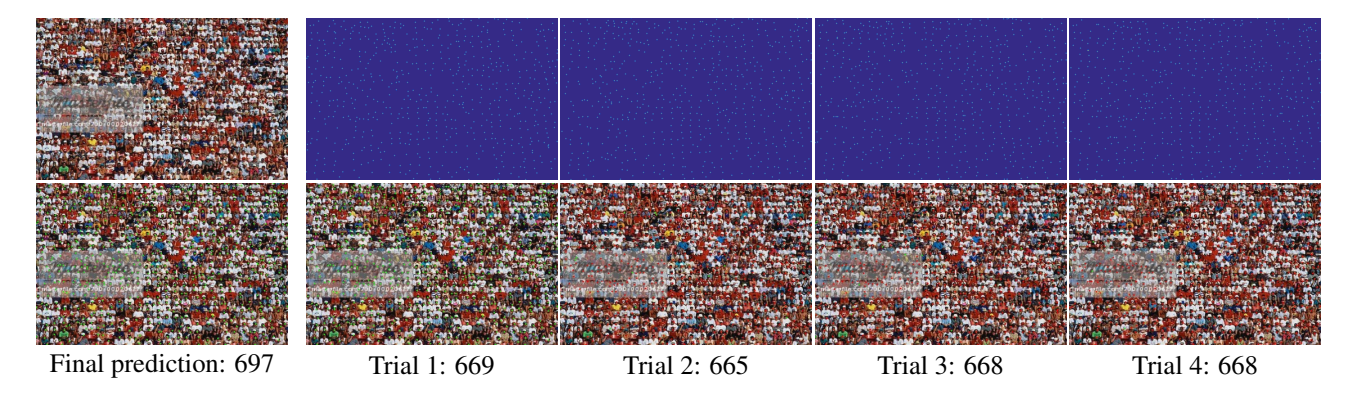


Figure 33. Additional qualitative results for crowd density maps and crowd maps for unlabeled images. The green dots in each individual trial represent the points included for the final prediction and the red dots are the rejected points.